The Notch1/CD22 signaling axis disrupts Treg cell function in SARS-CoV2-associated multisystem inflammatory syndrome in children

One Sentence Summary: Notch1-CD22 Axis Promotes Immune dysregulation in MIS-C

Mehdi Benamar[1,2], Qian Chen[1,2], Janet Chou[1,2*], Amélie M Julé[1,2,3*], Rafik Boudra[4], Paola Contini[5,6], Elena Crestani[1,2], Peggy S. Lai[7,8], Muyun Wang[1,2], Jason Fong[1,2], Shira Rockwitz[9], Pui Lee[1,2], Tsz Man Fion Chan[1,2], Ekin Zeynep Altun[10], Eda Kepenekli[11], Elif Karakoc-Aydiner[12], Ahmet Ozen[12], Perran Boran[13], Fatih Aygun[14], Pinar Onal[14], Ayse Ayzit Kilinc Sakalli[14], Haluk Cokugras[14], Metin Yusuf Gelmez[15], Fatma Betul Oktelik[15], Esin Aktas Cetin[15], Yuelin Zhong[1,2], Maria Lucia Taylor[1,2], Katherine Irby[16], Natasha B. Halasa[17], Elizabeth H Mack[18] Overcoming COVID-19 Investigators[19], Sara Signa[20], Ignazia Prigione[21], Marco Gattorno[21], Nicola Cotugno[22.23], Donato Amodio[22], Raif S. Geha[1,2], Mary Beth Son[1,2], Jane Newburger[24,2] Pankaj B. Agrawal[25,9,2], Stefano Volpi[20], Paolo Palma[22,23], Ayca Kiykim[26], Adrienne G. Randolph[27,2], Gunnur Deniz[15], Safa Baris[12], Raffaele De Palma[5,28,29], Klaus Schmitz-Abe[1,2,9], Louis-Marie Charbonnier[1,2], Lauren A. Henderson[1,2], Talal A. Chatila[1,2,30]

[1]Division of Immunology, Boston Children’s Hospital, Boston, Massachusetts, USA; [2]Department of Pediatrics, Harvard Medical School, Boston, Massachusetts, USA; [3]Department of Biostatistics, Harvard T.H. Chan School of Public Health, Boston, MA,USA [4]Brigham and Women Hospital, department of dermatology, Harvard Medical School, Boston, Massachusetts, USA, [5]Unit of Clinical Immunology and Translational Medicine, IRCCS Ospedale Policlinico San Martino, Genoa, Italy; [6] Department of Cardiology, Boston Children’s Hospital, Boston, Massachusetts, USA [7]Division of

Pulmonary and Critical Care, Massachusetts General Hospital, Boston, Massachusetts, USA; [8]Department of Medicine, Harvard Medical School, Boston, Massachusetts, USA; [9] The Manton Center for Orphan Disease Research, Boston Children's Hospital, Boston, USA [10] Ministry of Healthy, Marmara University Education and Training Hospital, Department of Pediatrics, Istanbul, Turkey; [11] Marmara University, Faculty of Medicine, Division of Pediatric Infectious Diseases, Istanbul, Turkey, [10] Marmara University, Faculty of Medicine, [12]Division of Pediatric Allergy and Immunology. The Isil Berat Barlan Center for Translational Medicine, Istanbul, Turkey, [13] Marmara University, Faculty of Medicine, Division of Social Pediatrics, Istanbul, Turkey [14] Division of Pediatric Allergy and Immunology, Faculty of Medicine, Istanbul University-Cerrahpasa, Istanbul, Turkey, [15]Department of Immunology, Aziz Sancar Institute of Experimental Medicine (Aziz Sancar DETAE), Istanbul University, Istanbul, Turkey; [16] Arkansas Children's Hospital, Little Rock, [17] Division of Pediatric Infectious Diseases, Department of Pediatrics, Vanderbilt University Medical Center, [18] Division of Pediatric Critical Care Medicine, Medical University of South Carolina, Charleston.[19]A complete list of the Overcoming COVID-19 Investigators is provided in the Supplementary, [20]DINOGMI, Università degli Studi di Genova, Genova, Italy and Center for Autoinflammatory Diseases and Immunodeficiencies, IRCCS Istituto Giannina Gaslini, Genova, Italy, [21] Center for Autoinflammatory Diseases and Immunodeficiencies, IRCCS Istituto Giannina Gaslini, Genova, Italy, [22] Clinical and Research Unit of Clinical Immunology and Vaccinology, Bambino Gesù Children's Hospital, IRCCS, Rome, Italy,[23] Chair of Pediatrics, Department of Systems Medicine, University of Rome "Tor Vergata", Roma, Italy. [24] Department of Cardiology, Boston Children's Hospital, Boston, Massachusetts, USA, [25]Division of

Newborn Medicine and Genetics & Genomics, Department of Pediatrics, Boston Children's Hospital, Harvard Medical School, Boston, Massachusetts, USA [26] Division of Pediatric Allergy and Immunology, Faculty of Medicine, Istanbul University-Cerrahpasa, Istanbul, Turkey; [27] Department of Anesthesiology, Critical Care, and Pain Medicine, Boston Children's Hospital, Boston, Massachusetts, USA; [28]Department of Internal Medicine (DIMI)-University of Genoa, Genoa; [29]CNR-Institute of Biomolecular Chemistry (IBC), Via Campi Flegrei 34, 80078 Pozzuoli, Napoli, Italy;

[30]Lead Contact

* These authors contributed equally

Corresponding Author: Talal A. Chatila, M.D., M.Sc.**,** Division of Immunology, Boston Children’s Hospital**,** Department of Pediatrics, Harvard Medical School, Boston, MA, USA.

Email: talal.chatila@childrens.harvard.edu

Abstract

Multisystem inflammatory syndrome in children (MIS-C) evolves in some pediatric patients following acute infection with SARS-CoV-2 by hitherto unknown mechanisms. Whereas acute-COVID-19 severity and outcome were previously correlated with Notch4 expression on regulatory T (Treg) cells, here we show that the Treg cells in MIS-C are destabilized through a Notch1-dependent mechanism. Genetic analysis revealed that MIS-C patients were enriched in rare deleterious variants impacting inflammation and autoimmunity pathways, including dominant-negative mutations in the Notch1 regulators *NUMB* and *NUMBL* leading to Notch1 upregulation. Notch1 signaling in Treg cells induced CD22, leading to their destabilization in a mTORC1-dependent manner and to the promotion of systemic inflammation. These results establish a Notch1-CD22 signaling axis that disrupts Treg cell function in MIS-C and point to distinct immune checkpoints controlled by individual Treg cell Notch receptors that shape the inflammatory outcome in SARS-CoV-2 infection.

Introduction

COVID-19, caused by the severe acute respiratory syndrome coronavirus 2 (SARS-CoV-2), has resulted in massive morbidity and mortality worldwide (1, 2). Acute infection is associated in some subjects with pneumonia and marked hypoxia, leading to acute respiratory distress syndrome as well as other life-threatening complications (3-5). This inflammation critically involves a dysregulated immune response characterized by intense activation of innate and adaptive immunity associated with features of a cytokine storm (6, 7). While most patients recover from this acute infection, a subset develops persistent symptoms related to different organ system dysfunction including the respiratory, cardiovascular, gastrointestinal, renal, and central nervous systems (8).

A special case in point is the course of SARS-CoV-2 infection in children. While most children remain asymptomatic or develop mild infection, some develop a multi-system inflammatory syndrome in children (MIS-C) approximately one month after initial infection (9-13). These patients exhibit severe immune dysregulation characterized by intense cytokine production and lymphocyte activation associated with fever and end-organ dysfunction including mucocutaneous, cardiovascular, hematologic, and especially gastrointestinal systems (14-21). IFNγ has been identified as a key cytokine in MIS-C with increased levels associated with disease severity and organ system involvement (22-25). The patients also exhibit robust T cells activation with T cell receptor repertoire skewing (24-29). There are defining characteristics of MIS-C that remain perplexing, including the substantial delay between the initial SARS-CoV-2 infection and MIS-C (9, 10, 12). Unlike children with acute COVID-19 pneumonia, most patients with MIS-C are previously healthy and are able to mount a robust immune response to SARS-CoV-2 with neutralizing antibodies to the virus (11, 18, 30). This constellation of features in MIS-C suggests that an evolving hyperinflammatory immune response to SARS-CoV-2 is part of the pathophysiology of this syndrome. Indeed, studies based on relatively small number of patients suggest that a genetic predisposition may contribute to the immune dysregulation in MIS-C (31, 32).

Notch signaling pathways have emerged as important regulators of the immune system by influencing both Treg and Tconv cells responses (33, 34). In mammals, the Notch family is composed by 4 Notch receptors (Notch1–4) and 5 ligands (Delta-like1, 3, and 4 and Jagged1 and 2) (35). Recent studies have outlined a prominent role for NOTCH4 in the immune dysregulation in acute COVID19 and related respiratory viral illnesses (36). Notch4 is upregulated on lung tissue Treg cells in an IL-6-dependent manner to subvert their tissue repair function in favor of an inflammatory response (36-39). The *NOTCH4* locus is associated with critical illness in COVID-19 (40). However, the immune dysregulatory mechanisms operative in post-acute COVID19 syndromes including MIS-C remain unclear.

In this study, we show that MIS-C patients exhibit robust T cells activation in association with increased Notch signaling in Treg cells. In particular, while NOTCH4 is also upregulated on circulating Treg cells of children with acute COVID19 as a function of disease severity, the Treg cells in MIS-C additionally upregulate NOTCH1 expression, a pathway previously implicated in T helper cell type 1 (Th1)-skewed immune dysregulation, autoimmunity, graft versus host disease and solid organ rejection (41, 42). Gene enrichment using whole genome/exome sequence analysis employing Fisher testing and Monte-Carlo simulation revealed the enrichment in MIS-C patients of rare mutations impacting pathways of inflammation and autoimmunity, many of which contained Notch-related genes. Consistent with these results, loss of function mutations were identified in the negative NOTCH1 regulators *NUMB* and *NUMBL* (43). In vitro experiment revealed that this loss of function mutations promotes Notch1 expression. Moreover, in mice either expressing an active form of Notch1 in Treg cells (*Foxp3*$^{\text{EGFPCre}}$*R26*$^{\text{N1c/+}}$) or lacking NUMB expression in these cells (*Foxp3*$^{\text{EGFPCre}}$*Numb*$^{\Delta/\Delta}$), treatment with Poly I:C to simulate viral infection induced systemic inflammation. Notch1 signaling in Treg cells induced the B cell inhibitory receptor CD22 (44, 45), which promoted systemic inflammation in association with the expression of the $\alpha4\beta7$ gut homing receptor. CD22 destabilized Treg cells and impaired their suppressive function in an mTORC1-dependent manner. Treatment of *Foxp3*$^{\text{EGFPCre}}$*R26*$^{\text{N1c/+}}$ or *Foxp3*$^{\text{EGFPCre}}$*Numb*$^{\Delta/\Delta}$ mice with an anti-CD22 mAb suppressed the development of systemic inflammation following Poly I:C treatment by restoring the Treg cells suppressive function. These findings point to the mobilization of Treg cell-specific tissue inflammatory licensing modules involving different Notch receptors that is operative in MIS-C and point to interventions along the Notch1-CD22 axis as therapeutic strategy in MIS-C.

Results

Increased CD4$^+$ T cell activation and Treg cell destabilization in MIS-C. To elucidate the immune dysregulatory mechanisms operative in MIS-C, we studied an international cohort of 45 children with MIS-C and 50 children with COVID-19 from centers in the United States, Italy and Turkey (**Table S1 and Patient Cohorts section in Methods**). For comparison, 5 children with Kawasaki disease (KD), 12 adults with COVID-19, and 18 pediatric healthy controls were also evaluated. All MIS-C patients met the Centers for Disease Control (CDC) Case Definition for MIS-C (46), while 93% fulfilled the WHO case definition (47-49). Fever was universal in MIS-C patients and rash (49%), conjunctivitis (58%), and GI symptoms (96%) were also common. Children with MIS-C were highly inflamed (median CRP 16.0 mg/dL, IQR 7.8-24.0), lymphopenic (median absolute lymphocyte count 0.91 x10^3/mL, IQR 0.53-1.35) and coagulopathic (median D-dimer 3.1 mcg/mL, IQR 1.5-6.2). Over 90% of MIS-C patients demonstrated positive SARS-CoV-2 serologies. 18/45 (40%) were considered to have severe MIS-C defined by admission to the intensive care unit (ICU), need for vasopressor support, and/or development of coronary artery aneurysms. The demographics and key clinical findings in the respective patient groups are delineated in **Table S1.**

To further delineate the CD4$^+$ T cell dynamics in MIS-C, we carried out single-cell RNA sequencing (scRNA-seq) analysis on CD4$^+$ T cells from the peripheral blood of four healthy controls, three MIS-C patients sampled prior to treatment and another five MIS-C patients sampled post-treatment. We first mapped our transcriptomic data to a reference human PBMC dataset using Azimuth (50), thereby delineating 6 subsets of CD4$^+$ T cells (**Fig. 1 A and B**). We further performed a graph-based clustering analysis using Seurat, which uncovered 16 clusters. Eight of these clusters (Clusters 1 to 8) were enriched in cells annotated as CD4 naïve by Azimuth and expressing genes associated with a naïve CD4$^+$ T cell profile (e.g., *CCR7* and *SELL*), 5 (Clusters 10 to 14) were enriched in activated CD4$^+$ T cells (*CD69*), including one with high NF-κB signaling (Cluster 10; *NFKB1*). The final 3 clusters encompassed a mix of naïve and activated cells, including one cluster delineated by viral sensing gene transcripts (Cluster 9; *IFIT2*, *IFIT3*), one cluster enriched in Treg cell transcripts (Cluster 15; *FOXP3*) and another with mitotic cells (Cluster 16; *TRBC1*) (**Fig. S1A-F**). Prior to treatment, MIS-C patients exhibited prominent expansion of cluster 10, enclosing both cells annotated as Tconv and Treg cells by Azimuth. Cluster 10 was characterized by increased *NFKB1* expression, and NF-κB signaling and contracted following immunomodulatory therapy (**Fig. S1A-F**).

To further decipher differences in CD4$^+$ T cell transcriptomic programs between patient groups, we also performed pseudobulk differential analysis (DEA) with a focus on both Treg (cells found in Cluster 15 or delineated as Treg cells by Azimuth) and Tconv cells (cells found in clusters 9 to 14 and delineated as activated Tconv by Azimuth). We aggregated gene expression data at the patient level for Treg cells and activated Tconv, and performed pairwise comparisons of MIS-C pre-treatment, post-treatment and control groups using DESeq2. The DEA were followed by gene set enrichment analyses (GSEA) against the MSigDB Hallmark collection and using the ranked log2 fold changes as input, which reinforced our prior observations of NF-kB pathway activation in pre-treatment MIS-C samples, not only in Tconv but also in Treg cells (**Fig. 1 C-H and Fig S1G-H)**. Pathways that were up regulated in the MIS-C pre-treatment group included mTORC1, whose hyperactivity has been previously noted to mediate Treg cell destabilization (**Fig. 1 C-H**

and Fig S1G-H) (51, 52). These results indicated that MIS-C is associated with enhanced Tconv activation and Treg dysregulation.

Increased NOTCH1 expression on CD4$^+$ Treg and Tconv cells in MIS-C. Previous studies have demonstrated a key role for Notch signaling-mediated Treg cell dysregulation in licensing tissue inflammation (36, 38, 41, 42). For example, NOTCH4 is upregulated in lung tissue Treg cells during SARS-CoV2 and influenza infections, leading to enhanced tissue inflammation and disease severity (36). We analyzed the expression of different Notch receptors on CD4$^+$ Treg and Tconv cells in pediatric subjects with mild and severe COVID19 and those with MIS-C. As comparison groups we included healthy children, adults with severe COVID19 and children with KD, some of whose clinical features overlap with those of MIS-C (16, 31, 48, 49). There was marked increase in NOTCH1 expression on both Treg and Tconv cells of patients with MIS-C but not on those of other subject groups (**Fig. 2A-C, Fig S2A**). NOTCH4 expression was also selectively increased on the circulating Treg cells of adult and pediatric subjects with severe COVID-19 and with MIS-C but not on their Tconv cells. NOTCH4 was also not upregulated on Treg cells of patients with mild COVID19 or with KD (**Fig. 2D-F, Fig S2B**). NOTCH1 expression in MISC was associated with increased intracellular expression of NOTCH1 cytoplasmic domain (N1c) in Treg cell (**Fig. 2G**). In contrast, NOTCH2 expression was increased on NOTCH1$^+$ Treg and Tconv cells of MIS-C subjects albeit at a lower magnitude than that of NOTCH1, while there was no difference in the NOTCH2 single positive Treg and Tconv cell populations between MIS-C and healthy controls (**Fig. S2C, Fig. S3 A and B, E-F).** Expression of NOTCH1 and NOTCH4 on Treg cells of MIS-C patients was non-overlapping, suggesting that they may represent distinct Treg cell populations possibly arising in different tissues (**Fig. S3E-F**). Also, there was no difference in NOTCH3 expression between the circulating Treg and Tconv cells of different patient populations and control subjects (**Fig. S2D and Fig. S3C and D**). Overall, these results identified increased NOTCH1 expression on Treg and Tconv cells as a distinguishing feature of pediatric patients with MIS-C.

Further analysis revealed that MIS-C patients present a decrease of naive Tconv and Treg cells associated with an increase of activated T cells (**Fig. S4 A to B**). As in previous studies (7), we found increased serum levels of IP-10, IL-1β, IL-6 and IFNλ2/3 in MIS-C and in severe COVID-19 compared to controls (**Fig. 2H**). Also, Treg and Tconv cells of patients with MIS-C versus severe COVID-19, KD and control subjects had increased IFN-γ production (**Fig. S4, C and D**). Notably, IFN-γ expression was selectively increased in Treg cells of MIS-C subjects, while IFN-γ expression in Tconv cells was common to both severe COVID-19 and MIS-C (**Fig. S4, C and D**). We analyzed the capacity of different cytokines found increased in the sera of MIS-C subjects to induce NOTCH1 expression on cell-sorted $CD4^{+}CD25^{+}CD127^{-}$ human Treg cells from control subjects. IL-1β and IL-6, and to a lesser extent IFN-γ and IP-10 all induced increased NOTCH1 expression on human Treg cells (**Fig. 2I**). MISC patients from North America and Europe were overall closely matched in their immunological analyses, with only differences found in NOTCH4, IP-10 and IFNL1 between these two cohorts (**Fig.S5 A-F**). Together, these results linked the upregulation of NOTCH1 expression on $CD4^{+}$ Treg and Tconv cells with the development of MIS-C.

Identification of Notch pathway genetic variants in MIS-C. To investigate underlying genetic factors that may predispose to MIS-C versus acute pediatric COVID-19, we performed gene-enrichment tests for rare variants (stop-gain/start-loss, frameshift deletions/insertions and canonical splicing mutations) using 8626 pathways from Gene-Ontology (GO) and Kyoto Encyclopedia of Genes and Genomes (KEGG) databases (8,299 and 327 respectively). We collected genome and exome sequences on 39 MIS-C and 24 acute pediatric COVID-19 subjects, which we compared with 8 different datasets comprising 4,682 exomes collected at the Boston Children's Hospital, including 4 rare disease categories, obesity, myopathy, autism-ADHD and Immune deficiency/dysregulation (53) (see Methods section). All samples were processed using the Variant Explorer (VExP) Pipeline with the same set parameters to avoid bias in the selection of the rare variants (54). We performed a Fisher test for each group to test for enrichment in the respective GO and KEGG pathways. Furthermore, we validated these results by Monte-Carlo simulation testing as an unbiased stochastic approach to test for enrichment in genetic variants along individual pathways in the MIS-C group versus the sum total of the clinical comparison groups used for the Fisher tests, as described in the Methods section. Several inflammation and autoimmunity pathways were significantly enriched in rare mutations (≤10 in 280,000 chromosomes) in MIS-C versus acute pediatric COVID-19 and the other comparison groups (**Fig. 3A and B, Dataset 1**). A number of those pathways contained NOTCH related genes. Specific NOTCH pathway mutations predicted to be damaging and linked to those pathways were identified included *NOTCH2*, *NOTCH4* and *RBPJL* (**Dataset 2**). Additionally, and in agreement with a previous report (55), we also detected rare heterozygous mutations in some genes associated with familial hemophagocytic lymphohistiocytosis, including *AP3B1, PRF1,* *LYST* and *DOCK8*, in patients with MIS-C (**Dataset 2**). Overall, these results supported the presence of an underlying genetic predisposition for MIS-C.

To validate the above findings from our initial cohort, we screened 88 additional patients with MIS-C from the U.S. multicenter Overcoming COVID-19 Network for mutations in Notch-related genes (see methods in Supplement) (9, 56). Rare damaging mutations were identified in *NUMB and NUMBL*, encoding closely conserved eponymous proteins that negatively regulate Notch receptor signaling and trafficking and which are expressed by human Treg and Tconv cells (**Fig S1D and E**) (43, 57-59). We further analyzed three mutations found in different patients that localized to the phosphotyrosine binding (PTB) domain of NUMB *(NM_001005745.1:c.280C>T; p.Leu94Phe), NUMBL (NM_004756.5:c.236G>T,NP_004747.1:p.Ser79Ile) and NUMBL (NM_004756.5:c.262G>A,NP_004747.1:p.Val88Met)* (**Fig. 4A and Dataset 3**). These mutations, which were either not found in the Genome Aggregation Database (gnomAD) (NUMB$^{\mathrm{Leu94Phe}}$ and NUMBL$^{\mathrm{Ser79Ile}}$; gnomAD=0) or very rarely so (NUMBL$^{\mathrm{Val88Met}}$; gnomAD=4), were predicted to impair NUMB and NUMBL regulatory functions (43, 58, 59). This prediction was tested by analyzing the impact of the respective NUMB/NUMBL mutations on NOTCH1 expression and function. Transgenic expression of the respective mutant protein in CRISPR-Cas9-generated NUMB/NUMBL-deficient human embryonic kidney 293 (HEK293) cells revealed that their expression was similar to wild-type NUMB (NUMB$^{\mathrm{WT}}$) and NUMBL (NUMBL$^{\mathrm{WT}}$) proteins (**Fig. 4B and C**). However, whereas transgenic NUMB$^{\mathrm{WT}}$ and NUMBL$^{\mathrm{WT}}$ decreased NOTCH1 expression in HEK293 cells, the NUMB$^{\mathrm{Leu94Phe}}$, NUMBL$^{\mathrm{Ser79Ile}}$ and NUMBL$^{\mathrm{Val88Met}}$ mutants failed to do so. Similarly, transgenic NUMB$^{\mathrm{WT}}$ and to a lesser extent NUMBL$^{\mathrm{WT}}$ decreased nuclear NOTCH1 cytoplasmic domain (N1c) expression whereas the mutant proteins failed to do so (**Fig. 4D and E**). Co-transfection studies revealed that the NUMB^{Leu94Phe} behaved as a dominant negative mutation that suppressed the capacity of NUMB^{WT} to decrease NOTCH1 and NOTCH1c expression (**Fig. 4D**). The NUMBL^{Ser79Ile} and NUMBL^{Val88Met} also behaved as dominant negative mutants in antagonizing the decrease in NOTCH1c (N1c) expression induced by NUMBL^{WT} (**Fig. 4 E**). Studies on the PBMCs of patients with the NUMB and NUMBL mutations showed upregulation of NOTCH1 expression on the Treg cells of all three patients (**Fig. S6 A-C**). Expression of N1c reflected the functional impact of these mutations as revealed in the vitro testing (**Fig. 4D and E)**, with the different mutations falling along a spectrum of NUMB^{Leu94Phe} > NUMBL^{Ser79Ile} > NUMBL^{Val88Met} (**Fig. S6 A-F)**. These results established that the identified NUMB/NUMBL mutations were functionally deleterious and that MIS-C subjects may harbor mutations in the Notch pathway that contribute to disease pathogenesis.

Poly I:C-induced multiorgan inflammatory disease in *Foxp3*^{EGFPCre}*R26*$^{N1c/+}$ mice. To further delineate the mechanisms by which increased NOTCH1 signaling in CD4$^+$ T cells promotes MIS-C, and in view of the critical role played by Treg cells in licensing Notch1-dependent immune dysregulation (41, 42), we employed a mouse model in which the intracellular domain of Notch1 (N1c) is conditionally expressed from the Rosa26 locus (*R26*$^{N1c/+}$) in Treg cells using a *Foxp3* promoter-regulated Cre recombinase fused with EGFP (*Foxp3*^{EGFPCre}) (**Fig. 5A**) (41). Treatment of *Foxp3*^{EGFPCre}*R26*$^{N1c/+}$ mice with polyinosinic:polycytidylic acid (Poly I:C), a proxy model of infection with RNA viruses (36, 60-62), resulted in progressive weight loss and multi-organ inflammation. In contrast, Poly I:C-treated control *Foxp3*^{EGFPCre} were minimally affected (**Fig. 5B-D**). Analysis of CD4$^+$ T cells of *Foxp3*$^{\text{EGFPCre}}$*R26*$^{\text{N1c/+}}$ mice revealed that their activation phenotype recapitulated that of CD4^{+} T cells of MIS-C patients, including increased memory markers (CD44^{+}CD62L^{-}) and heightened IFNγ production by both Treg and Tconv cells (**Fig. 5E-G**).

Most MIS-C patients present gastrointestinal symptoms (**Table S1**) (14) (13). Notably, the Treg and to a lesser extent the Tconv cells of the *Foxp3*$^{\text{EGFPCre}}$*R26*$^{\text{N1c/+}}$ mice had increased expression of the gut-homing integrin $\alpha4\beta7$ (**Fig. 5H)**. Increased expression of integrin $\alpha4\beta7$ (ITGB7) was also observed on the circulating Treg cells of MIS-C but not acute pediatric COVID-19 subjects, in agreement with a critical role of Notch1 in driving the expression of this marker (**Fig. 5I**). Consistent with this finding, MIS-C patients exhibited an increase in CD62L^{-}CD38^{+} mucosally imprinted Treg cells (**Fig. S7A**) (63, 64). sc-RNA seq analysis demonstrated increased *ITGB7* transcripts (**Fig. 5J and Fig. S7B**). Expression of integrin $\alpha4\beta7$ on Treg cells of MIS-C subjects declined post-treatment, in synchrony with decreased Notch1 and CD22 expression (**Fig. 5K-M**). These results indicated that increased Notch1 activity in Treg cells predisposes to multi-organ inflammation in the context of a viral trigger and promotes Treg cell gut homing.

Notch1-mediated CD22 upregulation on Treg cells promotes multi-organ inflammation. To delineate the mechanisms by which Notch1 signaling in Treg cells promotes multi organ inflammation in the context of a viral trigger, we analyzed the transcriptome of Notch1c-expressing Treg cells for pathways involved in the immune dysregulation (41). We found upregulation of CD22, a member of the Siglec family of lectins normally found in B cells, where it acts to regulate B cell receptor signaling (45). In particular, CD22 directs B cells to the intestinal lymphoid and mucosal tissues by upregulating the expression of the gut homing receptor $\alpha4\beta7$ (44). Flow cytometric analysis of Treg cells of *Foxp3*^{EGFPCre}*R26*$^{N1c/+}$ mice revealed increased CD22 expression upon treatment of the mice with Poly I:C (**Fig. 6A**). Expression of CD22 in Treg cells was abrogated upon Treg cell-specific deletion of *Rbpj,* the gene encoding the Notch canonical pathway transcriptional co-factor RBPJ (**Fig. S8A**). Analysis of peripheral blood Treg cells of MIS-C subjects revealed increased expression of CD22 that strongly correlated with NOTCH1 expression on these cells (**Fig. 6B**). CD22 expression was also increased in patients with NUMB/NUMBL mutations in accord with the impact of the mutation (**Fig. S6 G-I)**. In contrast, CD22 was minimally expressed on CD4$^+$ Tconv cells of control, acute COVID-19 and MIS-C subjects, and it did not correlate with Notch1 expression on these cells signaling (**Fig. 6B and C**). These results indicated that CD22 was upregulated on Treg cells with active NOTCH1 signaling.

The functional relevance of CD22 expression on Treg cells was analyzed by performing *in vitro* Treg cell suppression assays on Treg cells pooled from different mice, which revealed profoundly defective suppressive function of CD22$^+$ Treg cells of *Foxp3*^{EGFPCre}*R26*$^{N1c/+}$ mice compared to Treg cells of *Foxp3*^{EGFPCre} control mice. This defect was corrected upon treatment of Treg cells with the anti-CD22 mAb (**Fig. 6D)**. Similarly, the suppressive function of MIS-C Treg cells was profoundly deficient compared to that of Treg cells of healthy controls, which was corrected upon treatment of the cells with the anti-CD22 mAb (**Fig. 6E**).

To determine the role of CD22 expression on Treg cells in the multi organ inflammatory disease triggered by Poly I:C treatment of *Foxp3*^{EGFPCre}*R26*$^{N1c/+}$ mice, we examined the impact of therapy with a neutralizing anti-CD22 mAb on disease outcome in these mice.

Anti-CD22 mAb treatment prevented the weight loss and the multi-organ inflammation induced by Poly I:C treatment (**Fig. 7A-C**). It downregulated the activation of splenic $CD44^+CD62L^-$ Tconv cells and the expression by Treg and Tconv cells of IFNγ (**Fig. 7C-F**). Anti-CD22 mAb treatment also downregulated the expression by splenic Treg cells of $\alpha4\beta7$ (**Fig. 7F**). Anti-CD22 mAb treatment did not deplete Treg cells (**Fig. 7G**). In contrast, B cell depletion with an anti-B cell specific anti-CD20 mAb failed on its own to protect against disease or to abrogate protection by anti-CD22 mAb treatment (**Fig. S8B and C**). Analysis of gut lamina propria lymphocytes (LPL) revealed increased infiltration with activated ($CD44^+CD62L^-$) Tconv and Treg cells with increased expression of IFNγ that was similarly downregulated upon treatment with the anti-CD22 mAb (**Fig. S8D and E**). Overall, these results indicated that anti-CD22 mAb treatment suppressed both the gut and systemic inflammation induced by Poly I:C treatment of *Foxp3*$^{\mathrm{EGFPCre}}$*R26*$^{\mathrm{N1c/+}}$ mice.

To further link the above results with our human studies, we employed another mouse model in which a floxed *Numb* allele was conditionally deleted in Treg cells (*Foxp3*$^{\mathrm{YFPCre}}$*NUMB*$^{\Delta/\Delta}$) (**Fig. S9A and B)**. Treatment of *Foxp3*$^{\mathrm{YFPCre}}$*NUMB*$^{\Delta/\Delta}$ mice with Poly I:C intraperitoneally resulted in progressive weight loss similar to what was observed in Poly I:C-treated *Foxp3*$^{\mathrm{EGFPCre}}$*R26*$^{\mathrm{N1c/+}}$ mice. In contrast, Poly I: C-treatment of control *Foxp3*$^{\mathrm{YFPCre}}$ had no effect (**Fig. S9C and D**). Analysis of $CD4^+$ T cells of *Foxp3*$^{\mathrm{YFPCre}}$*NUMB*$^{\Delta/\Delta}$ mice revealed that their activation phenotype recapitulated that of $CD4^+$ T cells of MIS-C patients, including increased memory markers ($CD44^+CD62L^-$) and heightened IFNγ production by Tconv cells (**Fig. S9E and F**). Moreover, Treg cells of Poly I:C-treated *Foxp3*$^{\mathrm{YFPCre}}$*NUMB*$^{\Delta/\Delta}$ mice also showed upregulation of Notch1, N1c, CD22 and $\alpha4\beta7$ that recapitulated the Treg cell phenotype of MIS-C patients and Poly

I:C-treated *Foxp3*$^{\text{EGFPCre}}$*R26*$^{\text{N1c/+}}$ mice (**Fig. S9G-J).** Finally, treatment of *Foxp3*$^{\text{YFPCre}}$*NUMB*$^{\Delta/\Delta}$ mice with an anti-CD22 mAb prevented disease development following Poly I:C treatment, downregulated Notch pathway and gut homing markers and suppressed CD4^{+} T cell expansion and activation and IFNγ expression in both the spleen and the gut (**Fig. S9A-M)**. Overall, these results indicated that Notch1-dependent induction of CD22 expression on Treg cells plays a crucial pro-inflammatory role in Poly I:C-treated *Foxp3*$^{\text{EGFPCre}}$*R26*$^{\text{N1c/+}}$ mice.

To determine the mechanisms by which CD22 subverted Treg cell function, we analyzed the steady state transcriptome of a pool of CD22^{+} Treg cells of *Foxp3*$^{\text{EGFPCre}}$*R26*$^{\text{N1c/+}}$ mice compared to control *Foxp3*$^{\text{EGFPCre}}$ Treg cells or CD22^{-} Treg cells of *Foxp3*$^{\text{EGFPCre}}$*R26*$^{\text{N1c/+}}$. KEGG/GO pathway analysis showed increased expression of genes involved in the regulation of the immune response, T cell migration and Notch signaling (**Fig. S10A-F**). Furthermore, we analyzed by flow cytometry the phenotypes of CD22^{+} colonic and splenic of Treg cells *Foxp3*$^{\text{EGFPCre}}$*R26*$^{\text{N1c/+}}$ mice isolated at steady state and following Poly I:C-treatment in comparison with those of Treg cells of similarly treated *Foxp3*$^{\text{EGFPCre}}$ mice. The CD22^{+} Treg cells exhibited decreased expression of Helios and NRP-1 both at steady state and after Poly I:C treatment in the face of similar expression of markers of T cell activation including CD44, suggesting their decreased stability (**Fig. S10G and H)**. In agreement with this conclusion, Foxp3 expression also decreased in CD22^{+} Treg cells following Poly I:C treatment. Treatment with anti-CD22 mAb reversed those defects in both colonic and splenic Treg cells (**Fig. 8A and Fig. S10H and I**).

CD22 regulates B cell receptor signaling by forming a molecular scaffold that enables coordinated docking of different downstream signaling pathways (65). Analysis of CD22^{+}

Treg cells revealed enhanced activation of T cell receptor-coupled pathways compared to control Treg cells, with increased phosphorylation of the extracellular signal-regulated kinases (ERK) and the phospholipase C gamma 1 (pPLCγ1) (**Fig. 8B)**. Downstream of the PI3-kinase pathway, phosphorylation of the kinase AKT at residue T308, a target of upstream phosphoinositide-dependent kinases, and the mammalian target of rapamycin complex 1 (mTORC1) substrate S6 kinase were also increased (**Fig. 8C)** (66, 67). Treatment with an anti-CD22 mAb downregulated S6 phosphorylation, thus indicating active intracellular signaling by CD22 in Treg cells (**Fig. 9A and B).** Anti-CD22 mAb treatment corrected the decreased MFI of Foxp3 found at the end of the In-vitro Treg suppressive assay, indicative of reversal of CD22$^+$ Treg cell instability (**Fig. 9C and D)**. Treatment with the mTOR inhibitor Rapamycin reversed the regulatory defect in CD22$^+$ Treg cells and the associated loss of Foxp3 expression (**Fig. 9E to G)**. These results indicated that CD22 positively enhanced T cell receptor signaling in Treg cells leading to their destabilization and loss of regulatory function by an mTORC1-dependent mechanism.

Discussion

In this study, we demonstrate that MIS-C entails the mobilization of a Treg cell-specific pathway involving Notch1-CD22 signaling that promotes immune dysregulation and which can be demonstrated both in human subjects and in proxy mouse models. Patients with MIS-C but not children or adults with acute COVID-19 demonstrated increased NOTCH1 expression on circulating CD4$^+$ Treg and Tconv cells, all of which declined precipitously following anti-inflammatory therapy. The pathogenic function of this pathway was confirmed by the identification of dominant negative mutations in PTB domains of *NUMB* and *NUMBL* in MIS-C subjects that resulted in increased NOTCH1 expression. It was also supported by the demonstration of a role for Notch pathway-related mutations in MIS-C using Monte Carlo simulation and Fisher Test. Uniquely, MIS-C subjects exhibited increased CD22 expression on Treg but not Tconv cells which could be demonstrated in mice to involve Notch1 signaling via the RBPJ-k canonical pathway. CD22 blockade was sufficient to inhibit the immune dysregulation triggered by Notch1 signaling in Treg cell in the Poly I:C proxy viral infection model, highlighting the critical role of this molecule in MIS-C disease pathogenesis.

Our previous studies have identified NOTCH4 to be specifically upregulated on circulating Treg cells in adult subjects with COVID-19; their origin could be traced in mouse models of viral infection to the lung (36). NOTCH4 was similarly upregulated on circulating Treg cells of pediatric subjects with acute COVID-19, while both NOTCH4 and NOTCH1 were upregulated on those of MIS-C subjects. However, expression of NOTCH1 and NOTCH4 on MIS-C Treg cells was mutually exclusive, suggesting that the respective Treg cell populations were ontogenically distinct. These findings suggest that NOTCH4 and

NOTCH1 regulate distinct checkpoints in the evolution of immune dysregulation following SARS-CoV-2 and other viral infections. Thus, NOTCH4 appears critical for licensing lung inflammation following SARS-CoV2, influenza and related viral infections (36). In contrast, increased NOTCH1 expression on Treg and Tconv cells, with at least some of the latter being derived from destabilized NOTCH1$^+$ Treg cells, may favor the evolution of Th1-skewed systemic inflammation (41, 42). Overall, our studies provide a mechanistic framework for the evolution of autoimmunity in MIS-C by establishing Notch pathway-dependent Treg cell dysfunction as a critical step in this process (16, 17, 25)

Mouse studies revealed that a critical step by which Notch1 signaling in Treg cells promotes systemic inflammation involves its induction of CD22, an inhibitory receptor previously associated with B cells, where it functions as a regulator of B cell receptor signaling. More recently, CD22 has been described to direct the homing of B cells to the gut lymphoid and mucosal tissues by virtue of its upregulation of the gut homing integrin $\alpha4\beta7$ (44). Consistent with these findings, treatment of mice whose Treg cells express a gain of function Notch1 mutant with an anti-CD22 blocking antibody rescued their gut and systemic inflammation following treatment with Poly I: C. CD22 impaired the *in vitro* Treg cell suppressive function, an effect that was reversed by treatment with the anti-CD22 blocking antibody. Notwithstanding its function as an inhibitory receptor, Treg cells expressing CD22 demonstrated increased T cell receptor signaling with increased mTORC1 activity, leading to defective Treg cell suppressive function that was reversed by treatment with the mTOR inhibitor rapamycin.

MIS-C is a rare complication of SARS-CoV-2 infection (68), suggesting a genetic predisposition to this disorder. In that regard, mutations in a number of immune regulatory genes have been described in MIS-C, including *SOCS1*, *XIAP* and *CYBB* as well as HLA-class I alleles and rare heterozygous mutations in genes associated with hemophagocytic lymphohistiocytosis (25, 27, 32, 55). We found variants in a number of Notch pathway genes in patients with MIS-C. Importantly, dominant negative loss of function mutations in *NUMB* and *NUMBL* found in MISC subjects resulted in increased NOTCH1 expression and NOTCH1 signaling, consistent with the pathogenic function of these mutations in this pathway in promoting MIS-C in the context of a systemic viral infection such as with SARS-CoV2.

Collectively, these results allow for the construction of a model that traces the evolution of MIS-C. An initial infection with the SARS-CoV2 virus results in the expansion of NOTCH4 and NOTCH1 Treg cells, the latter favored by rare genetic variants found in the susceptible host. A subset of NOTCH1$^+$ Treg cells upregulates CD22, which severely impairs their regulatory function and drives their homing to the gut where they promote inflammation, possibly instigated by persistence of SARS-CoV2 in the gastrointestinal tract and/or in reaction to the gut microbiota (14). This cascading immune dysregulatory process may be amplified by heightened responses among some children to pathogen- and damage-associated signals (21), which aggravates the systemic spread of inflammation and the broad disruption of tissue Treg cell function. Importantly, Notch-related immune dysregulation may extend to involve other disease states associated with inflammation including other viral infections, inflammatory bowel disease and graft versus host disease (41, 42, 44, 69). This dysregulation is reversible by anti-inflammatory therapy that targets cytokines involved in Notch1 induction. Our results also suggest that blockade of CD22 or treatment with the mTORC1/2 inhibitor rapamycin may provide an alternative therapy in those patients who prove resistant to standard of care anti-inflammatory therapy.

Acknowledgment

We would like to acknowledge David A. Williams, MD, Lucinda Williams, DNP, RN, PNP, Myriam Armont, PhD, Leah Cheng, MA and other research staff who made major contributions to the Taking on COVID-19 Together Study at Boston Children's Hospital. We would also like to acknowledge the patients and families who participated by contributing samples for these studies. We also thank the Harvard Bioinformatics Core members for their help with single-cell RNA-seq analysis. This work was supported by a National Institutes of Health (NIH) grants R01 AI115699, R01 AI065617, and R01 AI06561720S1 to T.A.C., NIH K08 AR073339, NIH P30 AR070253 and All Arthritis Grant from the Arthritis National Research Foundation (to L.A.H.), NIH R01DK1300465 to J.C. and R01AI139633 to R.S.G and by Istanbul University BAP Project number TOA-2020-35899 to G.D. Supported by Grant by Italian Ministry of University and Research (MUR) FISR2020IP_04530 to R.D.P. Supported by the U.S. Centers for Disease Control and Prevention Contract 75D30120C07725 (to A.G.R., J.C., N.B.H.). M.B is a recipient of a grant from the Office of Faculty Development at Boston Children's Hospital.

Authors Contributions.

M.B and T.A.C. conceived the project and designed experiments. M.B., Q.C, R.B., P.C., M. W, J.F, P.L, T.M.F, E.Z.A., E.K., E.K-A, A.O, P.B, F.A, P.O, A.A.K.S., H.C, M.Y.G, F.B.O, E.A.C, Y.Z, and L-M.C performed experiments. J.C., E.C., P.S.L, M.L.T, M.B.S., J.N, S.S., I.P., M.G. E.H.M., S.V., A.K., G.D, A.R., S.B, R.D.P and L.A.H. supervised patient recruitment and sample collection at the respective centers. P.A provided group samples for the Fisher and Monte-Carlo analysis. L.A.H. J.C and A.G.R collected and analyzed clinical data. J.C., A.G.R., S.R, and R.S.G organized the preparation of whole exome/genome sequencing and J.C. K.S.A analyzed whole exome sequencing data. K.S.A. analyzed the RNA-seq data and performed the genetic analysis. L.A.H and A.M.J conceived the sc-RNA-seq experiments and A.J. analyzed the sc-RNA-seq data. K.S.A. analyzed the RNA-seq data, performed the genetic study and the design/processing/analysis for the Monte Carlo method and Fisher test. MB and T.A.C. wrote the manuscript.

Supplementary Materials

Fig S1–7

Datasets 1-3

Declaration of Interest: T.A.C., M.B., P.S.L., P.C. and R.D.P. are inventors on provisional patent application US 63/038,186 titled “Methods and Compositions for treating coronavirus infectious disease”. T.A.C. is co-founder of and hold equity in Alcea Therapeutics. LAH had received salary support from the Childhood Arthritis and Rheumatology Research Alliance (CARRA); consulting fees from Sobi, Pfizer, and Adaptive Biotechnologies; and investigator-initiated grant support from Bristol Myers Squibb.

Experimental Procedures

Patient Cohorts Contributing to the Flow Cytometry, Transcriptomic, and Functional Studies:

MIS-C and Pediatric COVID-19: Peripheral blood samples were obtained from children with COVID-19 (n=9) and MIS-C (n=23) who were prospectively recruited from Boston Children's Hospital (BCH) as part of the Taking on COVID-19 Together Study and the Kawasaki Disease (KD) Biorepository between 5/2020 and 4/2021. In addition, blood samples were also collected from children cared for at the Marmara University Hospital in Istanbul, Turkey (8 COVID-19, 8 MIS-C from 12/2020 to 1/2021), Istanbul University-Cerrahpaşa, Istanbul, Turkey (20 COVID-19, 2 MIS-C from 7/2020 to 1/2021), Gaslini Institute in Genoa, Italy (4 MIS-C from 12/2020 to 3/2021), and the Bambino Gesù Children's Hospital in Rome, Italy (13 COVID-19, 12 MIS-C from 3/2020 to 4/2021). The clinical characteristics of children with MIS-C and pediatric COVID-19 are reported in Table S1. All Patients with MIS-C met the Centers for Disease Control (CDC) Case Definition for MIS-C (46). Patients requiring intensive care unit (ICU) admission and/or vasopressor support or those who developed coronary artery aneurysms (z-score ≥ 2.5) were classified as having severe MIS-C.

Children with COVID-19 presented with either a fever, respiratory illness, and/or known COVID-19 exposure and were found to be SARS-CoV-2 positive by polymerase chain reaction (PCR). Moderate pediatric COVID-19 was defined by a supplemental oxygen requirement and care on the pediatric ward while severe disease required ICU admission and/or bilevel positive airway pressure (BiPAP) or mechanical ventilation. All other children with COVID-19 were defined as having mild cases.

Adult COVID-19: Twelve patients previously described (Harb et al, 2021) were used in this study.

Kawasaki Disease: Five children with KD provided peripheral blood samples through the KD Biorepository at BCH from 10/2020 to 1/2021 (Table 1). These patients fulfilled the clinical criteria for either complete or incomplete KD as outlined by the American Heart Association (AHA)(70). Further, all of these patients tested negative for SARS-CoV-2 by both PCR and serology and had no known close contacts with COVID-19.

Controls: Peripheral blood samples were obtained from pediatric control subjects recruited from Boston Children's Hospital (n=6), Istanbul University-Cerrahpaşa (n=7), and Gaslini Institute (n=5). Clinical characteristics of the control study subjects can be found in Table S1.

Sample Processing: Peripheral blood samples were obtained at study enrollment in either sodium heparin or EDTA tubes. At each site, PBMCs were isolated by Ficoll density gradient centrifugation and cryopreserved in liquid nitrogen.

Gene Pathway Analyses using the Fischer and Monte-Carlo tests. Whole genome or whole exome sequences were obtained from patients with MIS-C and children with COVID-19. These patients were recruited from the Taking on COVID-19 Together Study at Boston Children's Hospital (30 with MIS-C and 21 with COVID-19) as well as the Marmara University Hospital (9 with MIS-C and 3 with COVID-19).

In addition, whole exome and genome sequencing data obtained from 1,885 families (4682 samples) at the Manton Center for Orphan Disease Research were used for gene-enrichment test [Manton Center for Orphan Disease Research: https://www.mantonfoundation.org/]. Data were divided in 4 groups depending in their phenotypes: obesity (86 samples), myopathy (310 samples), autism-ADHD (1296 samples) or rare diseases (2990 samples). Rare diseases were subdivided depending on the sequencing provider, Broad Institute (1006 samples), GeneDx (715 samples), Boston Children's Hospital (545 samples) and others (724 samples). 162 families (385 samples) with immunodeficiency, allergic dysregulation, autoimmunity, and recurrent infections obtained from Boston Children's Hospital repositories were also included in our analysis.

Patient Screening for NOTCH-related Genes: Blood samples from patients with MIS-C enrolled in the Overcoming COVID-19 Immunobiology Study we obtained from 20 large pediatric sites in the U.S.A and were sent for whole exome sequencing (88 MIS-C from 6/2020 to 5/2021). DNA was isolated from whole blood using the Gentra Puregene Blood Kit (Qiagen) or by GeneDx using IDT xGen probes. Libraries for whole exome sequencing were prepared using Agilent Technologies SureSelectXT2 Homo Sapiens All Exon V6 Kit. Paired end sequencing was performed with an Illumina HiSeq-2000, generating 150 base reads. Sequencing alignment to the hg19/GRCh37 reference build was performed using the Burrows-Wheeler Aligner (71). Variant calling and candidate variant analysis were completed by utilizing the Boston Children's Hospital Genomic Learning System, as previously described (53). Minor allelic frequencies for the specified variants were identified by using the Genome Aggregation Database (72).

Mice. The following mouse strains were obtained from the JAX Laboratories: *Foxp3*$^{\mathrm{EGFPCre}}$ (B6129S-Tg (Foxp3-EGFP/icre)1aJbs/J), *Rosa26*$^{\mathrm{N1c/+}}$. *Rbpj1*$^{\mathrm{fl/fl}}$ (B6.129P2-*Rbpj*$^{\mathrm{tm1Hon}}$/HonRbrc) mice were a kind gift of Tasuku Honjo.

Single-cell RNA sequencing. Cryopreserved PBMCs were thawed in plain RPMI (HyClone) pre-warmed to 37°C, washed in PBS (HyClone) and resuspended in FACS buffer (PBS with 1.5% FBS (Genesee Scientific) and 2.5 mM EDTA (Invitrogen)) for CD4 T cell enrichment through negative selection (Miltenyi Biotec). Samples were studied in 2 independent experiments: experiment 1 included 3 pediatric controls, 1 pre-treatment MIS-C patient, and 4 post-treatment MIS-C patients; experiment 2 included 1 pediatric control, 2 pre-treatment MIS-C patients, and 1 post-treatment MIS-C patient. Detailed procedures are described in Supplemental Materials section.

Single-cell RNA sequencing clustering analyses. Sequencing data from each 10x run were processed with the CellRanger pipeline (10x Genomics) for demultiplexing and gene alignment (73). The resulting raw count matrices were imported in R (v4.0.2 and above) using Seurat (v4.0.3) (50). Data from all 3 runs were merged into one Seurat object. Genes detected in <1 per 10,000 cells were filtered out, leaving a transcriptomic coverage of 21,675 genes. High quality cells with >1400 unique molecular identifiers (UMIs), >700 genes, a log10(gene) to log10(UMI) ratio >0.84 and mitochondrial to nuclear gene ratio <0.08 were retained for downstream analyses. Quality control revealed no significant batch effect: similar distributions were observed for the metrics mentioned above across different runs and experiments. Detailed procedures are described in Supplemental Materials section.

Pseudobulk differential expression analyses (DEA). For pseudobulk differential expression analyses (DEA), gene expression level data was aggregated at the patient level for each subset of interest, namely Tregs and activated Tconv. For this analysis, we considered as Treg any cell assigned to Seurat Cluster 15 (*FOXP3*-expressing cells) or annotated as Treg by Azimuth, which added up to 1,925 Treg cells across all 12 patients. Similarly, we considered as activated Tconv any cell assigned to Seurat Clusters 9 to 14 and annotated as CD4 TCM, CD4 TEM, CD4 CTL or CD4 Proliferating by Azimuth (6,674 cells). Detailed procedures are described in Supplemental Materials section.

Gene pathway analysis using the Fischer and Monte-Carlo tests. To identify if a pathway is relevant to MIS-C or acute-COVID-19 (mild and severe pediatrics patients), a comparison between MIS-C or acute-COV19 and the eight databanks described above was performed as detailed in the Supplemental Materials section.

CRISPR/Cas9 Knock-out generation. HEK293 cells were transfected with CRISPR/Cas9 knockout plasmids NUMB/NUMBL (Santa Cruz Biotechnologies) using a CalPhos Mammalian Transfection kit (Takara), following the manufacturer protocol. CRISPR positive cells were isolated by FACS and plated at very low density to induce the formation of clonal colonies. Individual clones were then isolated and tested for knockout efficiency by flow cytometry.

***In vitro* NOTCH1 induction:** Human Treg cells from Healthy Donor were isolated by cell sorting (Sony Sorter, MA900) based on CD3, CD4, CD25^{high}, CD127^{Low}. Treg cells were seeded at 1×10^4 cells in 96-well plates then stimulated with CD3/CD28 Dynabeads (ThermoFisher) alone or in presence of recombinant IL-1β, IP-10, IL-6, IFN-γ and IFN-λ2 (10 µg /ml; Peprotech) for 72h. Notch1 expression on Foxp3$^+$ Treg cells was then assessed by Flow cytometry.

***NUMB* and *NUMBL* mutagenesis and cells transfection.** A plasmid pCMV6-AC-Numb-GFP encoding for human NUMB (NM_001005745) or human NUMBL (NM_004756*)* were purchased from OriGene (RG209744). The directed NUMB (c.280 C>T, p.Leu 94 Phe) and NUMBL (*c.236G>T, p.Ser79Ile; c.262G>A p.Val88Met)* mutagenesis plasmids were generated with standard cloning techniques by using pCMV6-AC-Numb-GFP as a template. NUMB/NUMBL-deficient HEK293T were cultured in 10% FBS DMEM medium (Gibco), supplemented with 100 U/mL penicillin, and 100 µg/mL streptomycin (Invitrogen). The day before transfection, the NUMB/NUMBL-deficient HEK293 cells were seeded at a density of 5x105 cells per well of 6 well plates. The next day, HEK293 cells were transiently transfected with 2 µg of the respective plasmids encoding either wild type or mutant NUMB or NUMBL using GeneJuice transfection reagent (Merck Millipore) according to the manufacturer's instructions. After 48h of transfection, cells were collected for Flow cytometry analysis.

Cytokine measurements. IL-1β, IL-6, IL-8, IFNα, IFNβ, IFNγ, IFNλ, CXCL10 and TNF were measured using Legendplex (Biolegend) per manufacturer's protocol.

Polyinosinic-polycytidylic acid (Poly I:C) mouse model. Mice were treated intraperitoneally with 2.5 mg/kg of Poly I:C HMW (InvivoGen) every two days for 12 consecutive days. The weight of the mice was recorded daily. Mice were euthanized and analyzed at day 13. For blockading CD22 mice were treated with an anti-CD22 antibody every two days for 12 consecutive days (InVivoMAb anti-mouse CD22; Clone: Cy34.1, Bioxcell). The antibody was given intra-peritoneally at 20 µg of antibody in PBS in a final volume of 100 µl or isotype control mAb (clone MOPC-21; Bioxcell). For the CD20 depletion experiment, the mice were given intraperitoneally 10µg of anti-CD20mAB (clone MB20-11; Bioxcell) or isotype control mAb (clone MOPC-21; Bioxcell) every 2 days, six days before the start of the experiment.

Histopathology staining. Paraffin-embedded lung, colon and liver sections were stained with hematoxylin and eosin (H&E) or Paraffin-acid-Schiff staining (PAS). The lung colon and liver pathology were scored by blinded operators, as described (74).

Flow cytometric analysis of mouse and human cells. Antibodies against murine and human antigens used for flow cytometric analyses are described in Table S2. The specificity and optimal dilution of each antibody were validated by testing on appropriate negative and positive controls or otherwise provided on the manufacturer's website. Intracellular cytokine staining was performed as previously described (41). Dead cells were routinely excluded from the analysis based on the staining of eFluor 780 Fixable Viability Dye (1:1000 dilution) (Thermofisher). Stained cells were analyzed on a BD LSR Fortessa cell analyzer (BD Biosciences) and data were processed using Flowjo (Tree Star Inc.).

Transcriptome Profiling. Treg cells were isolated from either *Foxp3*$^{\mathrm{EGFPcre}}$ or Foxp3$^{\mathrm{EGFPCre}}$ *Rosa26*$^{\mathrm{N1c/+}}$ mice by cell sorting, and their RNA was isolated using Qiagen RNeasy mini kit (Qiagen). RNA was then converted into double-stranded DNA (dsDNA), using SMART-Seq v4 Ultra Low Input RNA kit (Clontech). dsDNA was then fragmented to 200-300 bp size, using M220 Focused-ultrasonicator (Covaris), and utilized for construction of libraries for Illumina sequencing using KAPA Hyper Prep Kit (Kapa Biosystems). Libraries were then quantified using Qubit dsDNA HS (High Sensitivity) Assay Kit on Agilent High Sensitivity DNA Bioanalyzer. Detailed procedures are described in Supplementary Material section.

In vitro suppression assays. Mouse and human Treg cell suppressive assay were performed as described (74). Treg cells of *Foxp3*$^{\mathrm{EGFPcre}}$ and Foxp3$^{\mathrm{EGFPCre}}$ *Rosa26*$^{\mathrm{N1c/+}}$ mice were cell sorted based on CD4, YFP and/or CD22 expression and were used as suppressor cells. Responder cells were co-cultured with Treg cells, at a 1:1 ratio, and stimulated at 37ºC 5% CO2 for 3 days with 2 µg/ml of coated anti-CD3 and 1 µg/ml of soluble anti-CD28 in presence of increased dose of anti-CD22 mAb or Rapamycin in 96-well, round-bottomed plates in triplicates. For human suppression assays Treg cells ($CD3^+CD4^+CD127^-CD25^{High}$) and $CD4^+$ Tconv (responder) cells were isolated from PBMCs by cell sorting. Responder cells were co-cultured with Treg cells, at a 1:1 ratio, and stimulated at 37ºC 5% CO2 for 3 days with 2 µg/ml of coated anti-CD3 and 1 µg/ml of soluble anti-CD28 in presence of 1 µg/ml anti-CD22 mAb or 1 ng/ml Rapamycin in 96-well, round-bottomed plates in triplicates. The responder cells were then analyzed for CellTrace dye dilution by flow cytometry.

Analysis of TCR signaling by phosphoflow. Total spleen from either *Foxp3*^{EGFPCr}e or *Foxp3*^{EGFPCre}*R26*$^{N1c/N1c}$ mice were stimulated at 37°C in non-supplemented RPMI 1640 using pre- formed complexes of biotinylated anti-CD3 mAb (clone 145-2C11, BD, 30 µg/ml), anti-CD4 mAb (GK1.5, BD, 30 µg/ml) and streptavidin (60 µg/ml) during 1 to 5 min. Reaction was stopped and cells were permeabilized using a Foxp3/transcription factor staining buffer (eBiosciences) and Perm buffer III (BD Biosciences). Cells were stained with antibodies described in Table S2. Samples were acquired on a Fortessa cytometer (BD) and data were analyzed using the FlowJo software.

Statistical analysis. Student's two-tailed t-test, one- and two-way ANOVA and repeat measures two-way ANOVA with post-test analysis and log-rank test of groups were used to compare test groups, as indicated. Linear Regression was used for correlation analysis. For analysis of the human data, summary statistics were calculated using number (percentage) for binary and categorical data and mean (standard deviation) or median (interquartile range) for continuous data depending on the normality of the distribution.

Study approval.

Human Subjects: Written informed consent (and assent when appropriate) was provided by the participants, their health care proxy and for minor children from at least one parent or legal guardian. The single center research protocols were approved by the Institutional Review Boards (IRBs) at Boston Children's Hospital (IRB-P00035409 [Taking on COVID-19 Together], X10-01-0308, IRB-P00005723), Marmara University Hospital (224165), Istanbul University-Cerrahpasa (159066), the Gasilini Institute (egione Liguria ImmunoCOVID19" 0012337/20), and the Bambino Gesù Children's Hospital (2083_OPBG_2020), Boston Children's Hospital (P0021163, P00035489, P00035810, IRB-P00004759 and 04-09-113R). Boston Children's Hospital serves as the single IRB for the multicenter Overcoming COVID-19 Immunobiology Study (IRB-P00033157) and all enrolling sites IRBs reviewed and approved the protocol. The Rare disease cohorts research protocols were approved by the Institutional Review Boards (IRBs) at the Manton Center samples (10-02-0053).

Animal Studies: All animal studies were reviewed and approved by the Boston Children's Hospital office of Animal Care Resources.

Data Availability. Any data and materials to be shared will be released via a material transfer agreement. Bullk-RNA sequencing datasets have been deposited in the Gene Expression Omnibus: GEO: GSE186799.

References

1. Cucinotta D, and Vanelli M. WHO Declares COVID-19 a Pandemic. *Acta Biomed.* 2020;91(1):157-60.
2. Hu B, Guo H, Zhou P, and Shi ZL. Characteristics of SARS-CoV-2 and COVID-19. *Nat Rev Microbiol.* 2021;19(3):141-54.
3. Berlin DA, Gulick RM, and Martinez FJ. Severe Covid-19. *N Engl J Med.* 2020.
4. Zhou F, Yu T, Du R, Fan G, Liu Y, Liu Z, et al. Clinical course and risk factors for mortality of adult inpatients with COVID-19 in Wuhan, China: a retrospective cohort study. *Lancet.* 2020;395(10229):1054-62.
5. Richardson S, Hirsch JS, Narasimhan M, Crawford JM, McGinn T, Davidson KW, et al. Presenting Characteristics, Comorbidities, and Outcomes Among 5700 Patients Hospitalized With COVID-19 in the New York City Area. *JAMA.* 2020.
6. Lucas C, Wong P, Klein J, Castro TBR, Silva J, Sundaram M, et al. Longitudinal analyses reveal immunological misfiring in severe COVID-19. *Nature.* 2020;584(7821):463-9.
7. Henderson LA, Canna SW, Schulert GS, Volpi S, Lee PY, Kernan KF, et al. On the Alert for Cytokine Storm: Immunopathology in COVID-19. *Arthritis & rheumatology.* 2020;72(7):1059-63.
8. Nalbandian A, Sehgal K, Gupta A, Madhavan MV, McGroder C, Stevens JS, et al. Post-acute COVID-19 syndrome. *Nat Med.* 2021;27(4):601-15.
9. Feldstein LR, Rose EB, Horwitz SM, Collins JP, Newhams MM, Son MBF, et al. Multisystem Inflammatory Syndrome in U.S. Children and Adolescents. *N Engl J Med.* 2020;383(4):334-46.
10. Lee PY, Day-Lewis M, Henderson LA, Friedman KG, Lo J, Roberts JE, et al. Distinct clinical and immunological features of SARS-CoV-2-induced multisystem inflammatory syndrome in children. *J Clin Invest.* 2020;130(11):5942-50.
11. Rostad CA, Chahroudi A, Mantus G, Lapp SA, Teherani M, Macoy L, et al. Quantitative SARS-CoV-2 Serology in Children With Multisystem Inflammatory Syndrome (MIS-C). *Pediatrics.* 2020;146(6).
12. Dufort EM, Koumans EH, Chow EJ, Rosenthal EM, Muse A, Rowlands J, et al. Multisystem Inflammatory Syndrome in Children in New York State. *N Engl J Med.* 2020;383(4):347-58.
13. Feldstein LR, Tenforde MW, Friedman KG, Newhams M, Rose EB, Dapul H, et al. Characteristics and Outcomes of US Children and Adolescents With Multisystem Inflammatory Syndrome in Children (MIS-C) Compared With Severe Acute COVID-19. *JAMA.* 2021;325(11):1074-87.
14. Yonker LM, Gilboa T, Ogata AF, Senussi Y, Lazarovits R, Boribong BP, et al. Multisystem inflammatory syndrome in children is driven by zonulin-dependent loss of gut mucosal barrier. *J Clin Invest.* 2021;131(14).
15. Porritt RA, Binek A, Paschold L, Noval Rivas M, Mc Ardle A, Yonker LM, et al. The autoimmune signature of hyperinflammatory multisystem inflammatory syndrome in children. *J Clin Invest.* 2021.

16. Consiglio CR, Cotugno N, Sardh F, Pou C, Amodio D, Rodriguez L, et al. The Immunology of Multisystem Inflammatory Syndrome in Children with COVID-19. *Cell.* 2020;183(4):968-81 e7.

17. Ramaswamy A, Brodsky NN, Sumida TS, Comi M, Asashima H, Hoehn KB, et al. Immune dysregulation and autoreactivity correlate with disease severity in SARS-CoV-2-associated multisystem inflammatory syndrome in children. *Immunity.* 2021;54(5):1083-95 e7.

18. Gruber CN, Patel RS, Trachtman R, Lepow L, Amanat F, Krammer F, et al. Mapping Systemic Inflammation and Antibody Responses in Multisystem Inflammatory Syndrome in Children (MIS-C). *Cell.* 2020;183(4):982-95 e14.

19. Carter MJ, Fish M, Jennings A, Doores KJ, Wellman P, Seow J, et al. Peripheral immunophenotypes in children with multisystem inflammatory syndrome associated with SARS-CoV-2 infection. *Nat Med.* 2020;26(11):1701-7.

20. Vella LA, Giles JR, Baxter AE, Oldridge DA, Diorio C, Kuri-Cervantes L, et al. Deep immune profiling of MIS-C demonstrates marked but transient immune activation compared to adult and pediatric COVID-19. *Sci Immunol.* 2021;6(57).

21. Petrara MR, Bonfante F, Costenaro P, Cantarutti A, Carmona F, Ruffoni E, et al. Asymptomatic and Mild SARS-CoV-2 Infections Elicit Lower Immune Activation and Higher Specific Neutralizing Antibodies in Children Than in Adults. *Front Immunol.* 2021;12:741796.

22. Rodriguez-Smith JJ, Verweyen EL, Clay GM, Esteban YM, de Loizaga SR, Baker EJ, et al. Inflammatory biomarkers in COVID-19-associated multisystem inflammatory syndrome in children, Kawasaki disease, and macrophage activation syndrome: a cohort study. *Lancet Rheumatol.* 2021;3(8):e574-e84.

23. Esteve-Sole A, Anton J, Pino-Ramirez RM, Sanchez-Manubens J, Fumado V, Fortuny C, et al. Similarities and differences between the immunopathogenesis of COVID-19-related pediatric multisystem inflammatory syndrome and Kawasaki disease. *J Clin Invest.* 2021;131(6).

24. Hoste L, Roels L, Naesens L, Bosteels V, Vanhee S, Dupont S, et al. TIM3+ TRBV11-2 T cells and IFNgamma signature in patrolling monocytes and CD16+ NK cells delineate MIS-C. *J Exp Med.* 2022;219(2).

25. Sacco K, Castagnoli R, Vakkilainen S, Liu C, Delmonte OM, Oguz C, et al. Immunopathological signatures in multisystem inflammatory syndrome in children and pediatric COVID-19. *Nat Med.* 2022.

26. Moreews M, Le Gouge K, Khaldi-Plassart S, Pescarmona R, Mathieu AL, Malcus C, et al. Polyclonal expansion of TCR Vbeta 21.3(+) CD4(+) and CD8(+) T cells is a hallmark of Multisystem Inflammatory Syndrome in Children. *Sci Immunol.* 2021;6(59).

27. Porritt RA, Paschold L, Rivas MN, Cheng MH, Yonker LM, Chandnani H, et al. HLA class I-associated expansion of TRBV11-2 T cells in multisystem inflammatory syndrome in children. *J Clin Invest.* 2021;131(10).

28. Cheng MH, Zhang S, Porritt RA, Noval Rivas M, Paschold L, Willscher E, et al. Superantigenic character of an insert unique to SARS-CoV-2 spike supported by skewed TCR repertoire in patients with hyperinflammation. *Proc Natl Acad Sci U S A.* 2020;117(41):25254-62.

29. Lam KP, Chinas M, Jule AM, Taylor M, Ohashi M, Benamar M, et al. SARS-CoV-2-specific T cell responses in patients with multisystem inflammatory syndrome in children. *Clin Immunol.* 2022;243:109106.
30. Diorio C, Henrickson SE, Vella LA, McNerney KO, Chase J, Burudpakdee C, et al. Multisystem inflammatory syndrome in children and COVID-19 are distinct presentations of SARS-CoV-2. *J Clin Invest.* 2020;130(11):5967-75.
31. Sancho-Shimizu V, Brodin P, Cobat A, Biggs CM, Toubiana J, Lucas CL, et al. SARS-CoV-2-related MIS-C: A key to the viral and genetic causes of Kawasaki disease? *J Exp Med.* 2021;218(6).
32. Chou J, Platt CD, Habiballah S, Nguyen AA, Elkins M, Weeks S, et al. Mechanisms underlying genetic susceptibility to multisystem inflammatory syndrome in children (MIS-C). *J Allergy Clin Immunol.* 2021;148(3):732-8 e1.
33. Vanderbeck A, and Maillard I. Notch signaling at the crossroads of innate and adaptive immunity. *J Leukoc Biol.* 2021;109(3):535-48.
34. Amsen D, Helbig C, and Backer RA. Notch in T Cell Differentiation: All Things Considered. *Trends Immunol.* 2015;36(12):802-14.
35. Radtke F, Fasnacht N, and Macdonald HR. Notch signaling in the immune system. *Immunity.* 2010;32(1):14-27.
36. Harb H, Benamar M, Lai PS, Contini P, Griffith JW, Crestani E, et al. Notch4 signaling limits regulatory T-cell-mediated tissue repair and promotes severe lung inflammation in viral infections. *Immunity.* 2021;54(6):1186-99 e7.
37. Xia M, Harb H, Saffari A, Sioutas C, and Chatila TA. A Jagged 1-Notch 4 molecular switch mediates airway inflammation induced by ultrafine particles. *J Allergy Clin Immunol.* 2018;142(4):1243-56 e17.
38. Harb H, Stephen-Victor E, Crestani E, Benamar M, Massoud A, Cui Y, et al. A regulatory T cell Notch4-GDF15 axis licenses tissue inflammation in asthma. *Nat Immunol.* 2020;21(11):1359-70.
39. Benamar M, Harb H, Chen Q, Wang M, Chan TMF, Fong J, et al. A common IL-4 receptor variant promotes asthma severity via a Treg cell GRB2-IL-6-Notch4 circuit. *Allergy.* 2022.
40. Pairo-Castineira E, Clohisey S, Klaric L, Bretherick AD, Rawlik K, Pasko D, et al. Genetic mechanisms of critical illness in COVID-19. *Nature.* 2021;591(7848):92-8.
41. Charbonnier LM, Wang S, Georgiev P, Sefik E, and Chatila TA. Control of peripheral tolerance by regulatory T cell-intrinsic Notch signaling. *Nat Immunol.* 2015;16(11):1162-73.
42. Magee CN, Murakami N, Borges TJ, Shimizu T, Safa K, Ohori S, et al. Notch-1 Inhibition Promotes Immune Regulation in Transplantation Via Regulatory T Cell-Dependent Mechanisms. *Circulation.* 2019;140(10):846-63.
43. McGill MA, and McGlade CJ. Mammalian numb proteins promote Notch1 receptor ubiquitination and degradation of the Notch1 intracellular domain. *J Biol Chem.* 2003;278(25):23196-203.
44. Ballet R, Brennan M, Brandl C, Feng N, Berri J, Cheng J, et al. A CD22-Shp1 phosphatase axis controls integrin beta7 display and B cell function in mucosal immunity. *Nat Immunol.* 2021;22(3):381-90.

45. Clark EA, and Giltiay NV. CD22: A Regulator of Innate and Adaptive B Cell Responses and Autoimmunity. *Frontiers in immunology.* 2018;9:2235.

46. Prevention CfDCa. Multisystem Inflammatory Syndrome in Children (MIS-C) Associated with Coronavirus Disease 2019 (COVID-19). https://emergency.cdc.gov/han/2020/han00432.asp.

47. Organization WH. Multisystem inflammatory syndrome in children and adolescents with COVID-19. https://www.who.int/publications/i/item/multisystem-inflammatory-syndrome-in-children-and-adolescents-with-covid-19.

48. Whittaker E, Bamford A, Kenny J, Kaforou M, Jones CE, Shah P, et al. Clinical Characteristics of 58 Children With a Pediatric Inflammatory Multisystem Syndrome Temporally Associated With SARS-CoV-2. *JAMA.* 2020;324(3):259-69.

49. Verdoni L, Mazza A, Gervasoni A, Martelli L, Ruggeri M, Ciuffreda M, et al. An outbreak of severe Kawasaki-like disease at the Italian epicentre of the SARS-CoV-2 epidemic: an observational cohort study. *Lancet.* 2020;395(10239):1771-8.

50. Hao Y, Hao S, Andersen-Nissen E, Mauck WM, 3rd, Zheng S, Butler A, et al. Integrated analysis of multimodal single-cell data. *Cell.* 2021;184(13):3573-87 e29.

51. Apostolidis SA, Rodriguez-Rodriguez N, Suarez-Fueyo A, Dioufa N, Ozcan E, Crispin JC, et al. Phosphatase PP2A is requisite for the function of regulatory T cells. *Nat Immunol.* 2016;17(5):556-64.

52. Gerriets VA, Kishton RJ, Johnson MO, Cohen S, Siska PJ, Nichols AG, et al. Foxp3 and Toll-like receptor signaling balance Treg cell anabolic metabolism for suppression. *Nat Immunol.* 2016;17(12):1459-66.

53. Rockowitz S, LeCompte N, Carmack M, Quitadamo A, Wang L, Park M, et al. Children's rare disease cohorts: an integrative research and clinical genomics initiative. *NPJ Genom Med.* 2020;5:29.

54. Schmitz-Abe K, Li Q, Rosen SM, Nori N, Madden JA, Genetti CA, et al. Unique bioinformatic approach and comprehensive reanalysis improve diagnostic yield of clinical exomes. *Eur J Hum Genet.* 2019;27(9):1398-405.

55. Vagrecha A, Zhang M, Acharya S, Lozinsky S, Singer A, Levine C, et al. Hemophagocytic Lymphohistiocytosis Gene Variants in Multisystem Inflammatory Syndrome in Children. *Biology (Basel).* 2022;11(3).

56. Son MBF, Murray N, Friedman K, Young CC, Newhams MM, Feldstein LR, et al. Multisystem Inflammatory Syndrome in Children - Initial Therapy and Outcomes. *N Engl J Med.* 2021;385(1):23-34.

57. McGill MA, Dho SE, Weinmaster G, and McGlade CJ. Numb regulates post-endocytic trafficking and degradation of Notch1. *J Biol Chem.* 2009;284(39):26427-38.

58. Frise E, Knoblich JA, Younger-Shepherd S, Jan LY, and Jan YN. The Drosophila Numb protein inhibits signaling of the Notch receptor during cell-cell interaction in sensory organ lineage. *Proc Natl Acad Sci U S A.* 1996;93(21):11925-32.

59. Kircher M, Witten DM, Jain P, O'Roak BJ, Cooper GM, and Shendure J. A general framework for estimating the relative pathogenicity of human genetic variants. *Nat Genet.* 2014;46(3):310-5.

60. Broggi A, Ghosh S, Sposito B, Spreafico R, Balzarini F, Lo Cascio A, et al. Type III interferons disrupt the lung epithelial barrier upon viral recognition. *Science.* 2020;369(6504):706-12.

61. Iwasaki A, and Pillai PS. Innate immunity to influenza virus infection. *Nat Rev Immunol.* 2014;14(5):315-28.

62. Kato H, Takeuchi O, Sato S, Yoneyama M, Yamamoto M, Matsui K, et al. Differential roles of MDA5 and RIG-I helicases in the recognition of RNA viruses. *Nature.* 2006;441(7089):101-5.

63. du Pre MF, van Berkel LA, Raki M, van Leeuwen MA, de Ruiter LF, Broere F, et al. CD62L(neg)CD38(+) expression on circulating CD4(+) T cells identifies mucosally differentiated cells in protein fed mice and in human celiac disease patients and controls. *Am J Gastroenterol.* 2011;106(6):1147-59.

64. van Leeuwen MA, du Pre MF, van Wanrooij RL, de Ruiter LF, Raatgeep HR, Lindenbergh-Kortleve DJ, et al. Changes in natural Foxp3(+)Treg but not mucosally-imprinted CD62L(neg)CD38(+)Foxp3(+)Treg in the circulation of celiac disease patients. *PLoS One.* 2013;8(7):e68432.

65. Poe JC, Fujimoto M, Jansen PJ, Miller AS, and Tedder TF. CD22 forms a quaternary complex with SHIP, Grb2, and Shc. A pathway for regulation of B lymphocyte antigen receptor-induced calcium flux. *J Biol Chem.* 2000;275(23):17420-7.

66. Alessi DR, James SR, Downes CP, Holmes AB, Gaffney PR, Reese CB, et al. Characterization of a 3-phosphoinositide-dependent protein kinase which phosphorylates and activates protein kinase Balpha. *Curr Biol.* 1997;7(4):261-9.

67. Zeng H, Yang K, Cloer C, Neale G, Vogel P, and Chi H. mTORC1 couples immune signals and metabolic programming to establish T(reg)-cell function. *Nature.* 2013;499(7459):485-90.

68. Payne AB, Gilani Z, Godfred-Cato S, Belay ED, Feldstein LR, Patel MM, et al. Incidence of Multisystem Inflammatory Syndrome in Children Among US Persons Infected With SARS-CoV-2. *JAMA Netw Open.* 2021;4(6):e2116420.

69. Tran IT, Sandy AR, Carulli AJ, Ebens C, Chung J, Shan GT, et al. Blockade of individual Notch ligands and receptors controls graft-versus-host disease. *J Clin Invest.* 2013;123(4):1590-604.

70. McCrindle BW, Rowley AH, Newburger JW, Burns JC, Bolger AF, Gewitz M, et al. Diagnosis, Treatment, and Long-Term Management of Kawasaki Disease: A Scientific Statement for Health Professionals From the American Heart Association. *Circulation.* 2017;135(17):e927-e99.

71. Li H, and Durbin R. Fast and accurate short read alignment with Burrows-Wheeler transform. *Bioinformatics.* 2009;25(14):1754-60.

72. Karczewski KJ, Francioli LC, Tiao G, Cummings BB, Alfoldi J, Wang Q, et al. The mutational constraint spectrum quantified from variation in 141,456 humans. *Nature.* 2020;581(7809):434-43.

73. Zheng GX, Terry JM, Belgrader P, Ryvkin P, Bent ZW, Wilson R, et al. Massively parallel digital transcriptional profiling of single cells. *Nat Commun.* 2017;8:14049.

74. Charbonnier LM, Cui Y, Stephen-Victor E, Harb H, Lopez D, Bleesing JJ, et al. Functional reprogramming of regulatory T cells in the absence of Foxp3. *Nat Immunol.* 2019;20(9):1208-19.

Figures

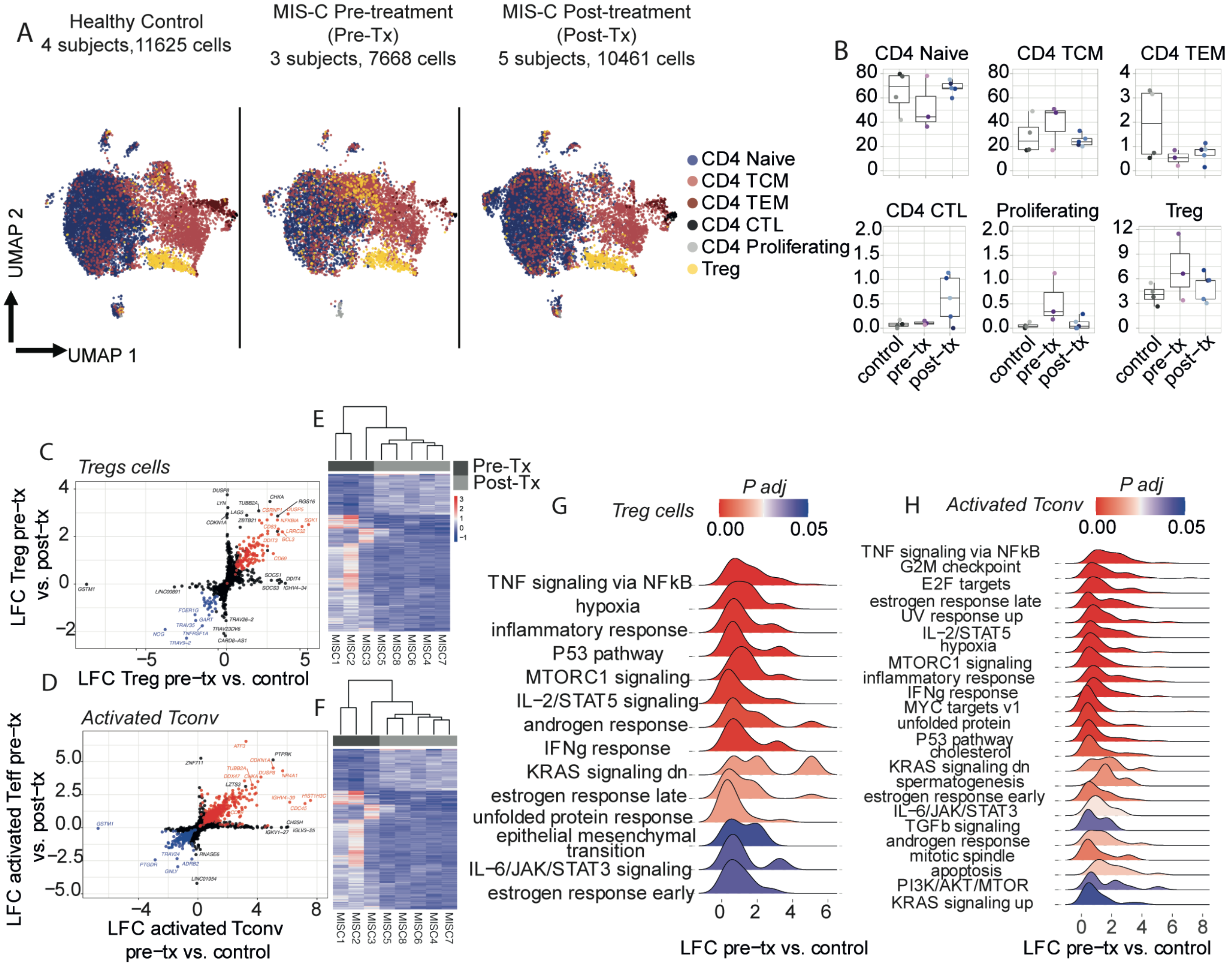

Figure 1. **Increased CD4 T cell activation and Treg cell destabilization in MIS-C**. Circulating CD4$^+$ T cells from control, pre- and post-treatment MIS-C subjects were studied with 10x Genomics. **A**. Uniform manifold approximation and projection (UMAP) of normalized and harmonized dataset, split by disease group and color-coded by cell type. Cell identities were defined by mapping the data to a reference human PBMC dataset with Azimuth. **B**. Frequencies (%) of each cell type among total CD4$^+$ T cells for each patient, as determined with scRNA-seq. **C, D**. Log2 fold changes (LFC) in gene expression derived from independent pseudobulk differential expression analyses (DEA) of pre-treatment MIS-C versus healthy control (x-axis) and of pre-treatment MIS-C versus

post-treatment MIS-C subjects (y-axis) in Treg cells (**C**) and Activated Tconv (**D**). For each cell type, genes differentially expressed (p-value < 0.2) in pre-treatment MIS-C versus both control and post-treatment subjects are highlighted (blue: LFC < 0, red: LFC > 0). **E, F**. Heatmaps of all genes found to be differentially expressed and significant (p-value < 0.05) in pseudobulk DEA of pre-treatment MIS-C versus either control or post-treatment subjects, respectively for Treg cells (**E**) and Activated Tconv (**F**). **G**, **H.** LFC distributions of genes belonging to each of the corresponding enriched hallmarks. Gene set enrichment analysis (GSEA) was run against the MSigDB hallmark database using ranked LFC derived from pseudobulk DEA of pre-treatment MIS-C versus control subjects in Treg cells.

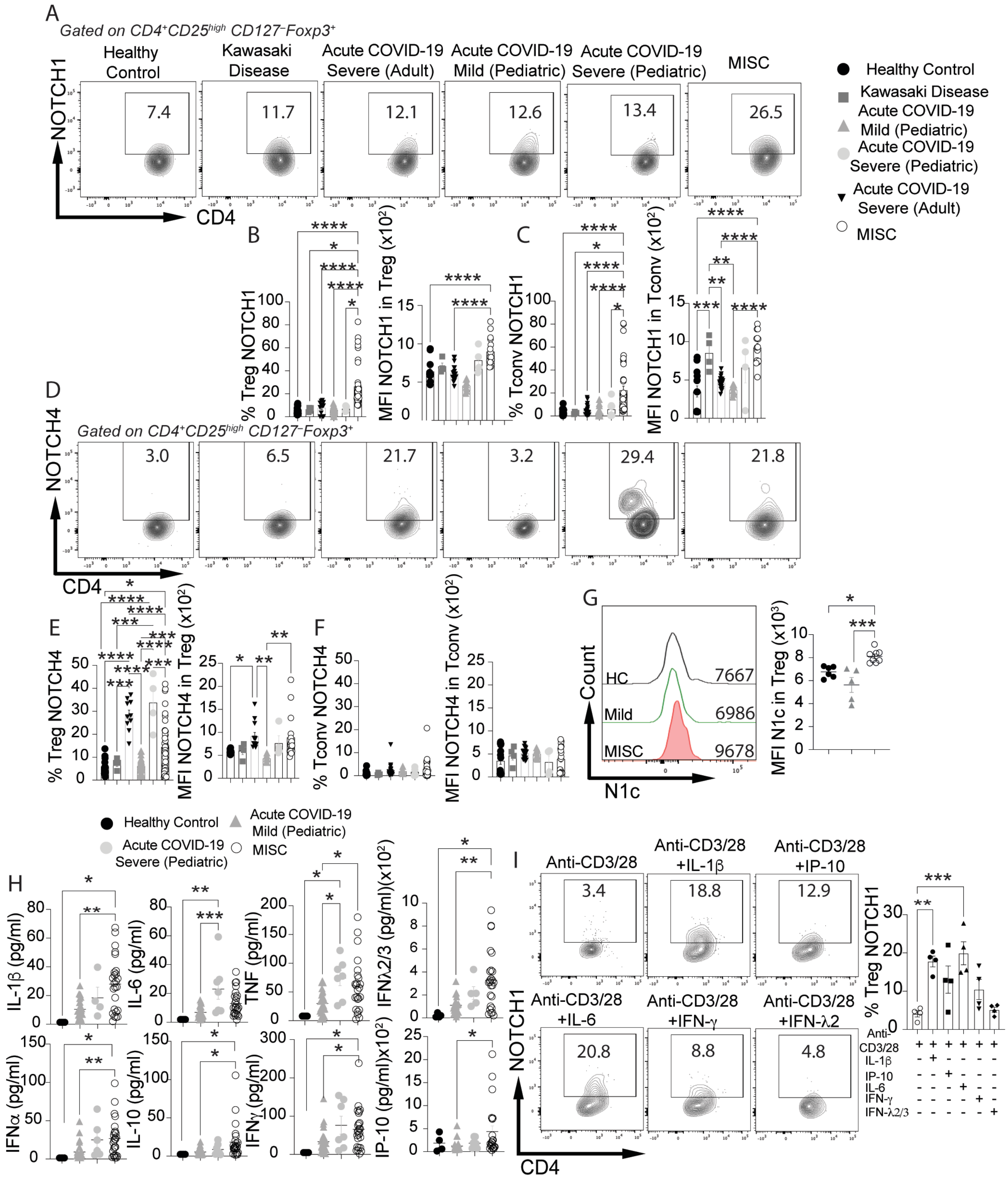

Figure 2. Increased Notch1 expression on circulating CD4$^+$ Treg and Tconv cells in MIS-C. A to F, Flow cytometric analysis, cell frequencies, and mean fluorescence intensity (MFI) of Notch1 (**A to C**) and Notch4 expression (**D to F**) in CD4$^+$ Treg and

Tconv cells of healthy control subjects, and patients with Kawasaki disease, adult subjects with severe COVID-19, pediatric subjects with mild or severe COVID-19 and MIS-C subjects. **G,** Flow cytometric analysis and mean fluorescence intensity (MFI) of N1c in $CD4^+$ Treg cells of healthy control subjects, and pediatric patients with severe COVID-19 or MIS-C. **H,** serum concentrations of IL-1β, IL-6, TNF, IFNα, IFNλ2/3, IFNγ IL-10, and IP-10 in control and the respective patient group subjects. **I**. Flow cytometric analysis and frequencies of Notch1 expression on anti-CD3-anti-CD28-activated $CD4^+$ human Treg cells treated with the respectively indicated cytokines. Each symbol represents one subject. Numbers in flow plots indicate percentages. Error bars indicate SEM. Statistical tests: $^*P<0.05$, $^{**}P<0.01$, $^{****}P<0.0001$ by one-way ANOVA with Dunnett's post hoc analysis (**A to E; H to I)**.

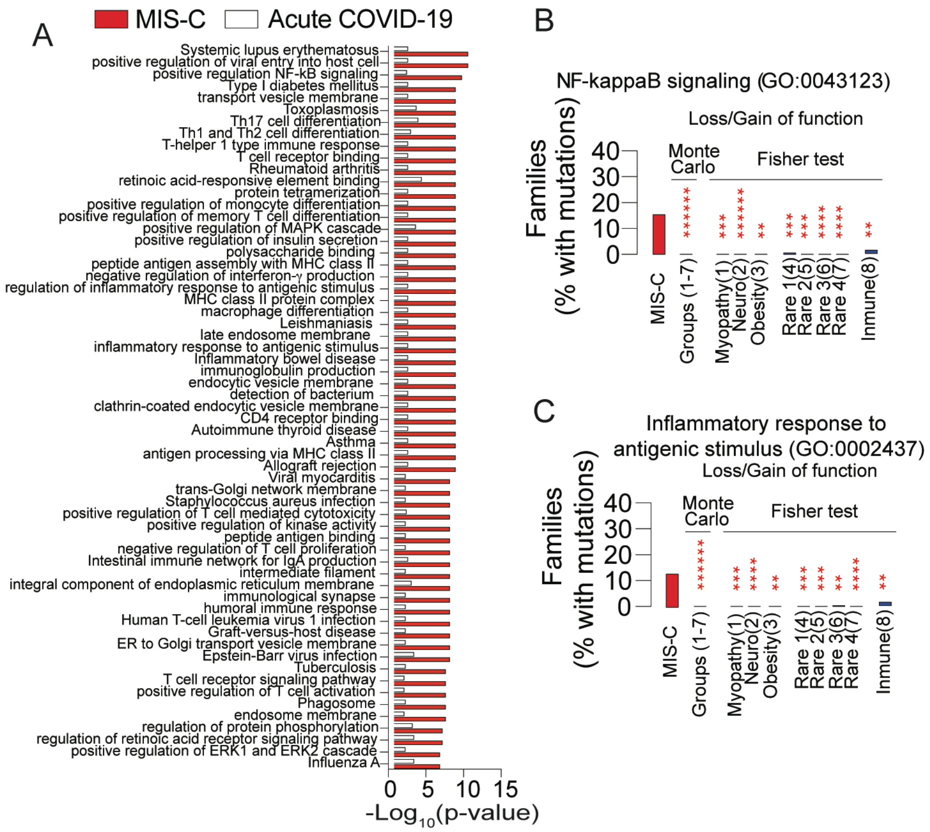

Figure 3: Identification of genetic pathway operative in MIS-C. **A.** KEGG and GO pathways differentially enriched in rare mutations in MIS-C versus Acute COVID-19 (severe and mild pediatrics patients) by Monte Carlo simulation and Fished Test as described in the Materials and Methods section. **B, C**. Frequency of mutations in two representative pathways: "positive regulation of NF-κB signaling"(**B**) and "inflammatory response to antigenic stimulus" (**C**), identified in A versus other disease groups either collectively by Monte Carlo simulation or individually by Fisher test. $^{**}P<0.01$, $^{***}P<0.001$, $^{****}P<0.0001$, $^{*****}P<0.00001$. by Monte Carlo simulation and Fished Test.

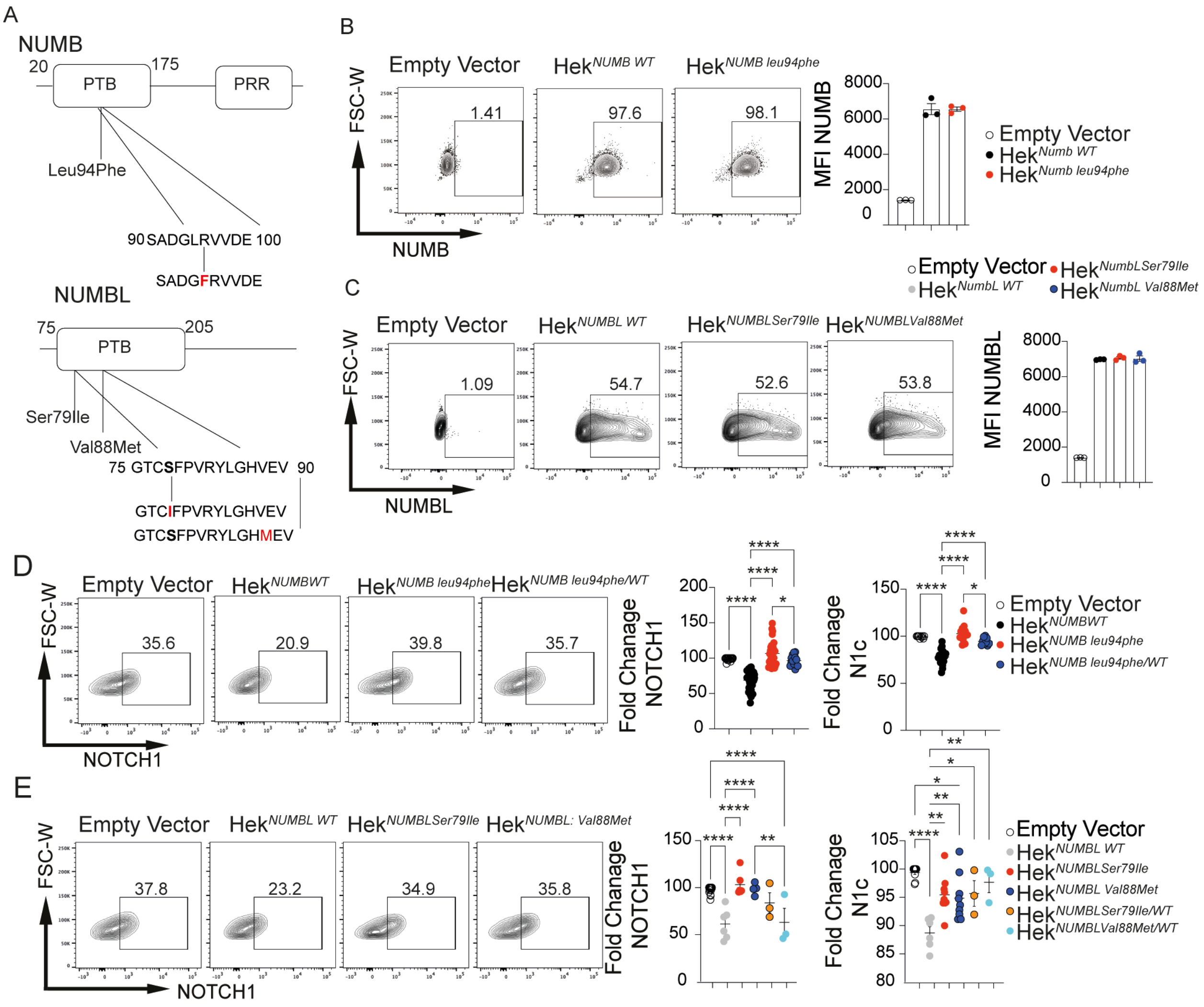

Figure 4: Identification of NUMB/NUMBL genetic variants in MIS-C: A. Schematic representation of *NUMB* and *NUMBL* mutations identified in MIS-C subjects. **B, C.** Expression of recombinant wild type NUMB protein (NUMB^{WT}) and NUMB^{Leu94Phe} (B), and NUMBL^{WT}, NUMBL^{Ser79Ile,} and NUMBL^{Val88Met} proteins (D) in NUMB/NUMBL-deficient HEK293 cells. **D and F.** Flow cytometric analysis and fold expression of NOTCH1 and N1c in NUMB/NUMBL-deficient HEK293 cell transfected with either NUMB^{Leu94Phe} (D), NUMBL^{Ser79Ile} or NUMBL^{Val88Met} proteins (F) either alone or together with the respective WT proteins. Error bars indicate SEM. Statistical tests for panels (**B to E**): *P<0.05,

**$P<0.01$, ***$P<0.001$, ****$P<0.0001$ by one-way ANOVA with Dunnett’s post hoc analysis.

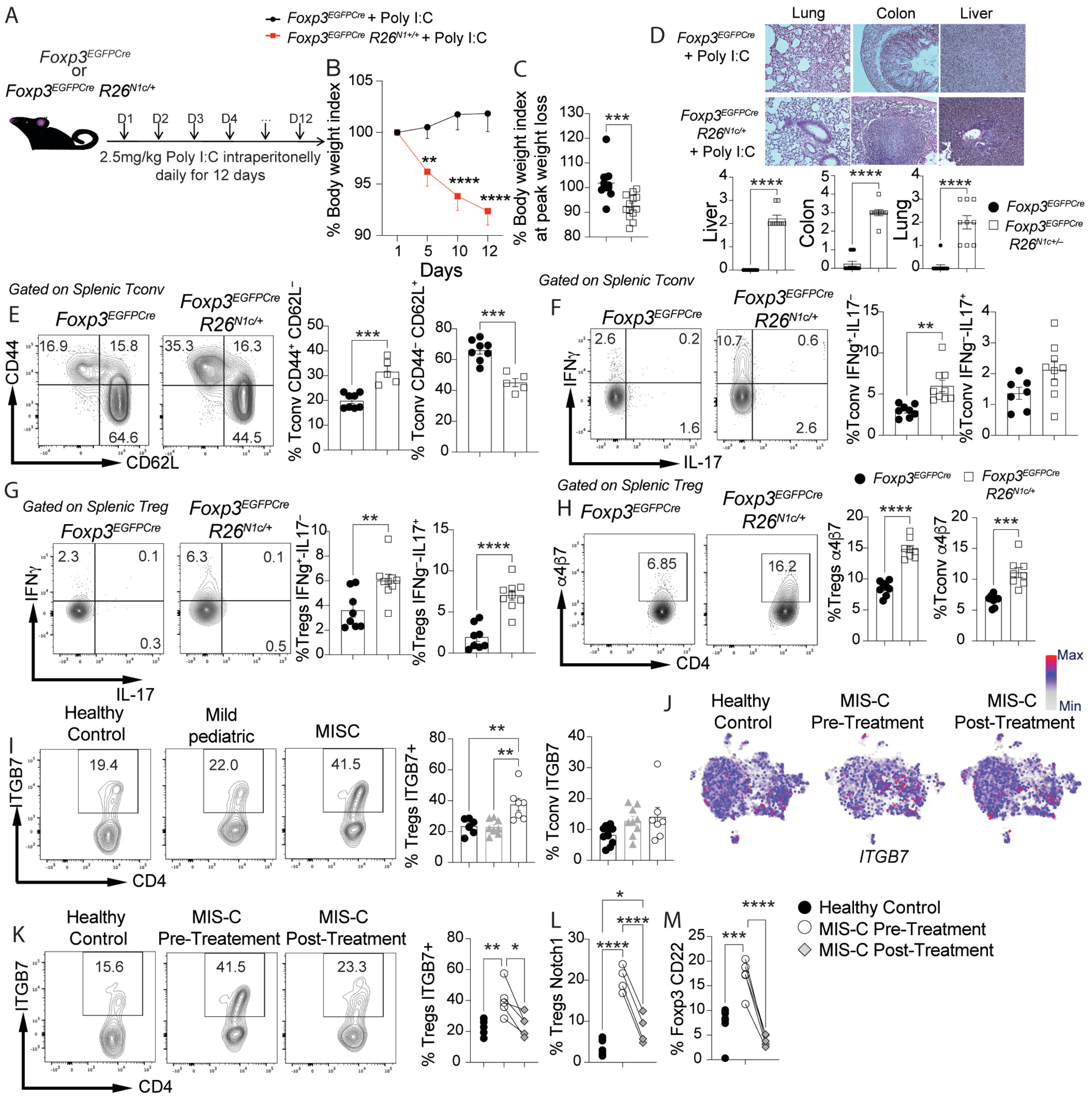

Figure 5. Poly I: C-induced multiorgan inflammatory disease in *Foxp3*$^{\text{EGFPCre}}$*R26*$^{\text{N1c/+}}$ mice. **A**. Experimental scheme. Mice were injected with Poly I: C intraperitoneally (i.p.) daily for 12 days. **B and C** Weight indices of *Foxp3*$^{\text{EGFPCre}}$ and *Foxp3*$^{\text{EGFPCre}}$*R26*$^{\text{N1c/+}}$ mice subjected to Poly I:C treatment. **D**, Hematoxylin and eosin-stained sections and inflammation score of liver, gut, and lung tissues isolated from the indicated mouse groups (×200 magnification). **E**. Flow cytometric analysis and graphical representation of

naïve ($CD4^+CD44^-CD62L^+$) and activated ($CD4^+CD44^+CD62L^-$) Tconv cells. **F and G**. Flow cytometric analysis and graphical representation of IFNγ and IL-17 expression in Tconv (**F**) and Treg cells (**G**) in the respective poly I: C-treated mouse groups. **H**. Flow cytometric analysis and graphical representation of $\alpha4\beta7$ expression in Treg and Tconv cells of the indicated mouse groups. **I**. Flow cytometric analysis and graphical representation of $\alpha4\beta7$ expression in Treg and Tconv cells of the indicated subject groups. **J**. Relative expression of *ITGB7* in the different clusters inferred from scRNA-seq data. **K**. Flow cytometric analysis and cell frequencies of $\alpha4\beta7$ (ITGB7) expression on circulating $CD4^+FOXP3^+$ Treg cells in healthy control subjects and in MIS-C patients pre and post-treatment. **L, M**. cell frequencies of Notch1(**L**) and CD22 (**M**) expression on circulating $CD4^+FOXP3^+$ Treg cells in healthy control subjects and in MIS-C patients pre and post-treatment. Each symbol represents one mouse (**B to I**), one cell (**J**), or one human subject (**I, K, L, M**). Numbers in flow plots indicate percentages. Error bars indicate SEM. Statistical tests: Two-way ANOVA with Sidak's post hoc analysis (**B**)**; Student T-test (C, D)** One-way ANOVA with Dunnett's post hoc analysis (**E to I, K, L, M**). *P<0.05, **P<0.01, ***P<0.001, ****P<0.0001.

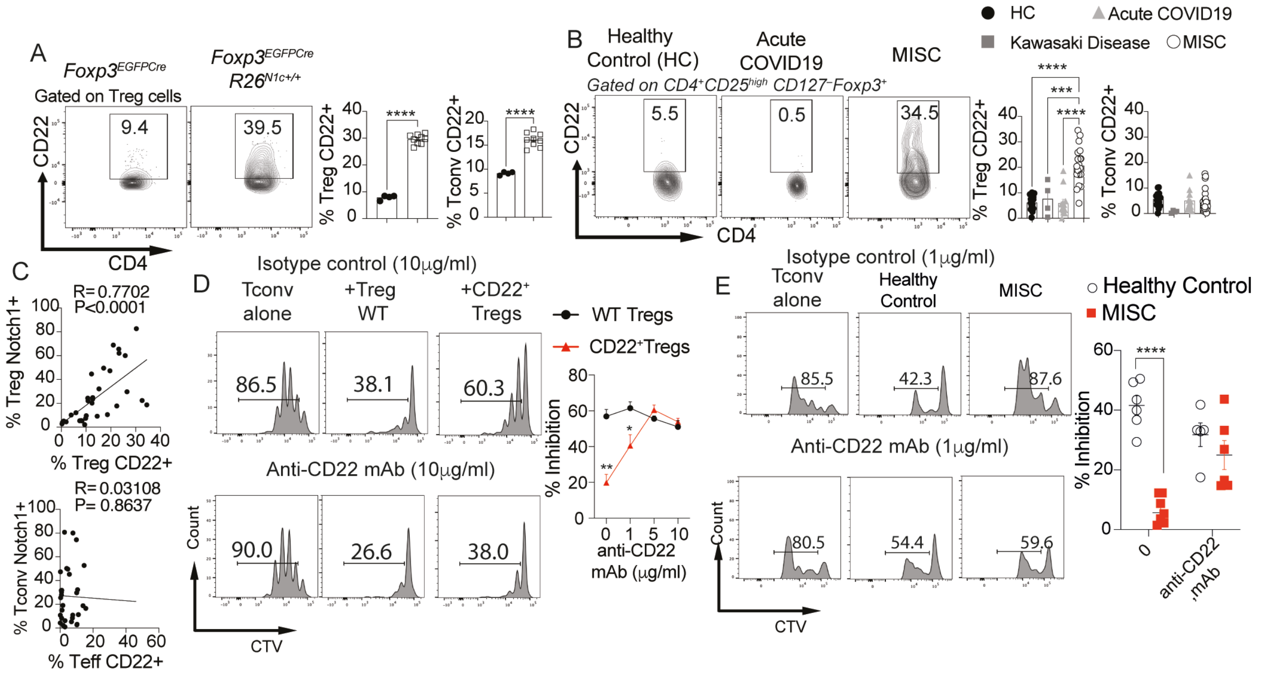

Figure 6. Notch1 destabilizes Treg suppressive function by a CD22-dependent mechanism. A. Flow cytometric analysis and graphical representation of CD22 expression in splenic Treg and Tconv cells of Poly I: C-treated *Foxp3*$^{\mathrm{EGFPCre}}$ and *Foxp3*$^{\mathrm{EGFPCre}}$*R26*$^{\mathrm{N1c/+}}$ mice. **B.** Flow cytometric analysis and cell frequencies of CD22 expression on circulating CD4$^+$FOXP3$^+$ Treg and CD4$^+$FOXP3$^-$ Tconv cells in healthy controls and in subjects with either mild pediatric COVID or MIS-C. **C**. Correlation analysis of CD22 expression on Treg and Tconv cells of MIS-C and control subjects as a function of Notch1 expression on these cells. **D** *In vitro* suppression of Tconv cell proliferation by *Foxp3*$^{\mathrm{EGFPCre}}$ and CD22$^+$ *Foxp3*$^{\mathrm{EGFPCre}}$*R26*$^{\mathrm{N1c/+}}$Treg cells in the presence of increasing concentrations of anti-CD22 mAb. **E** *In vitro* suppression of human Tconv cell proliferation by Treg cells isolated from healthy controls or MIS-C subjects either in the absence of presence of anti-CD22 mAb. Each symbol represents one mouse (A), or one human subject (B and C). Numbers in flow plots indicate percentages. Error bars indicate SEM. Statistical tests)**;** Student T-test **(A)** One-way ANOVA with Dunnett's post hoc analysis

(**B**); Two-way ANOVA with Sidak's post hoc analysis (D and E)**;** and Pearson correlation analysis (**C**). *P<0.05, **P<0.01, ***P<0.001, ****P<0.0001.

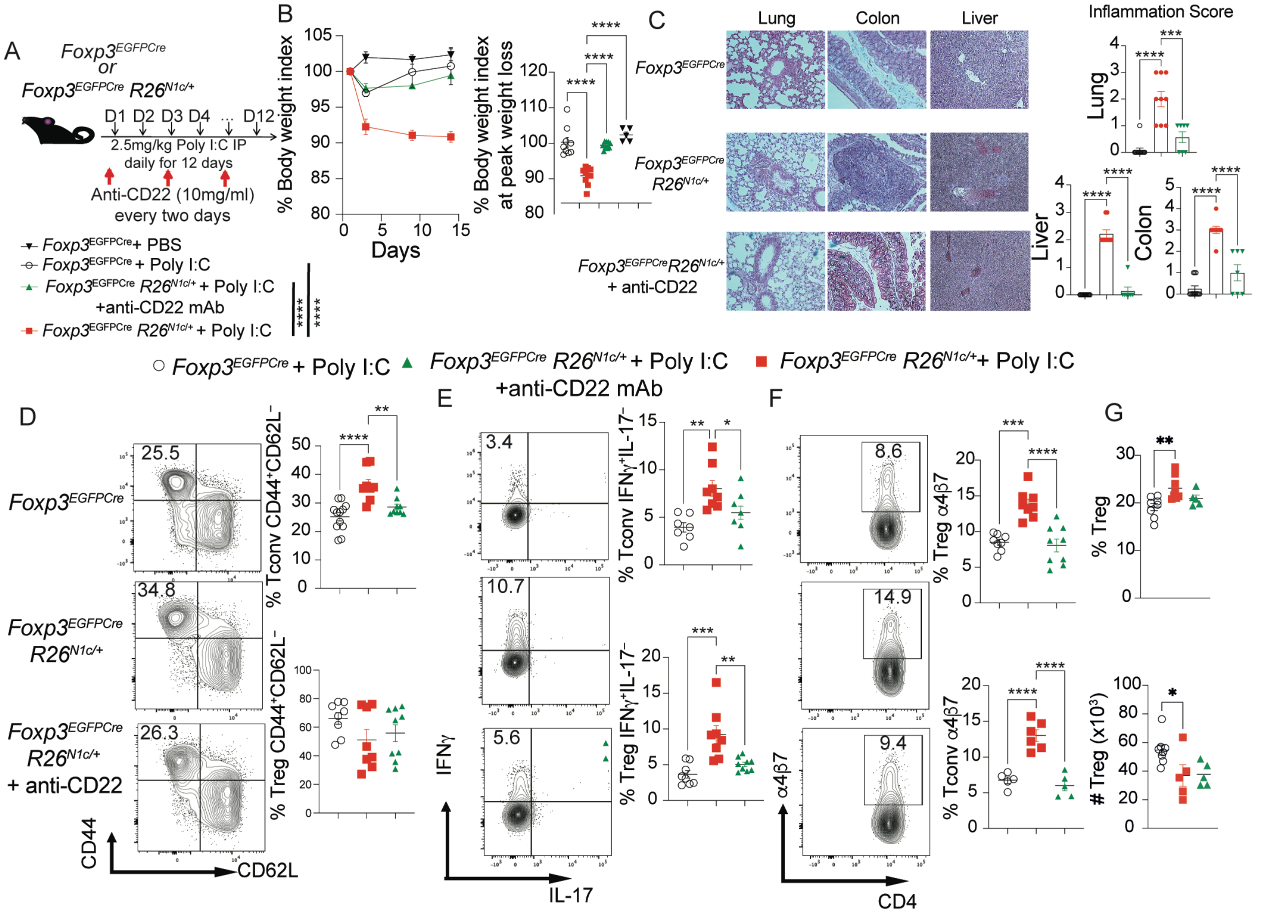

Figure 7: **A Treg cell Notch1-CD22 axis promotes multi-organ inflammation A.** Experimental scheme. Mice were injected with Poly I: C intraperitoneally (i.p.) daily for 12 days. **B,** Weight indices of *Foxp3*$^{\mathrm{EGFPCre}}$ and *Foxp3*$^{\mathrm{EGFPCre}}$*R26*$^{\mathrm{N1c/+}}$ mice subjected to Poly I:C treatment. **C,** Hematoxylin and eosin-stained sections and inflammation score of liver, gut, and lung tissues isolated from the indicated mouse groups (×200 magnification). **D,** Flow cytometric analysis and graphical representation of naïve ($\mathrm{CD4^+CD44^-CD62L^+}$) and activated ($\mathrm{CD4^+CD44^+CD62L^-}$) Tconv cells. **E,** Flow cytometric analysis and graphical representation of IFNγ and IL-17 expression in Tconv (E) and Treg cells (F) in the respective poly I: C-treated mouse groups. **F.** Flow cytometric analysis and graphical representation of α4β7 expression in Treg and Tconv cells of the indicated mouse groups.

G. Frequencies and cell number of Splenic Treg cells in the respective groups. Each symbol represents one mouse (B-H). Numbers in flow plots indicate percentages. Error bars indicate SEM. Statistical tests: Two-way ANOVA with Sidak's post hoc analysis (**b**)**;** One-way ANOVA with Dunnett's post hoc analysis (**B,C,D,E,F,G**); *P<0.05, **P<0.01, ***P<0.001, ****P<0.0001.

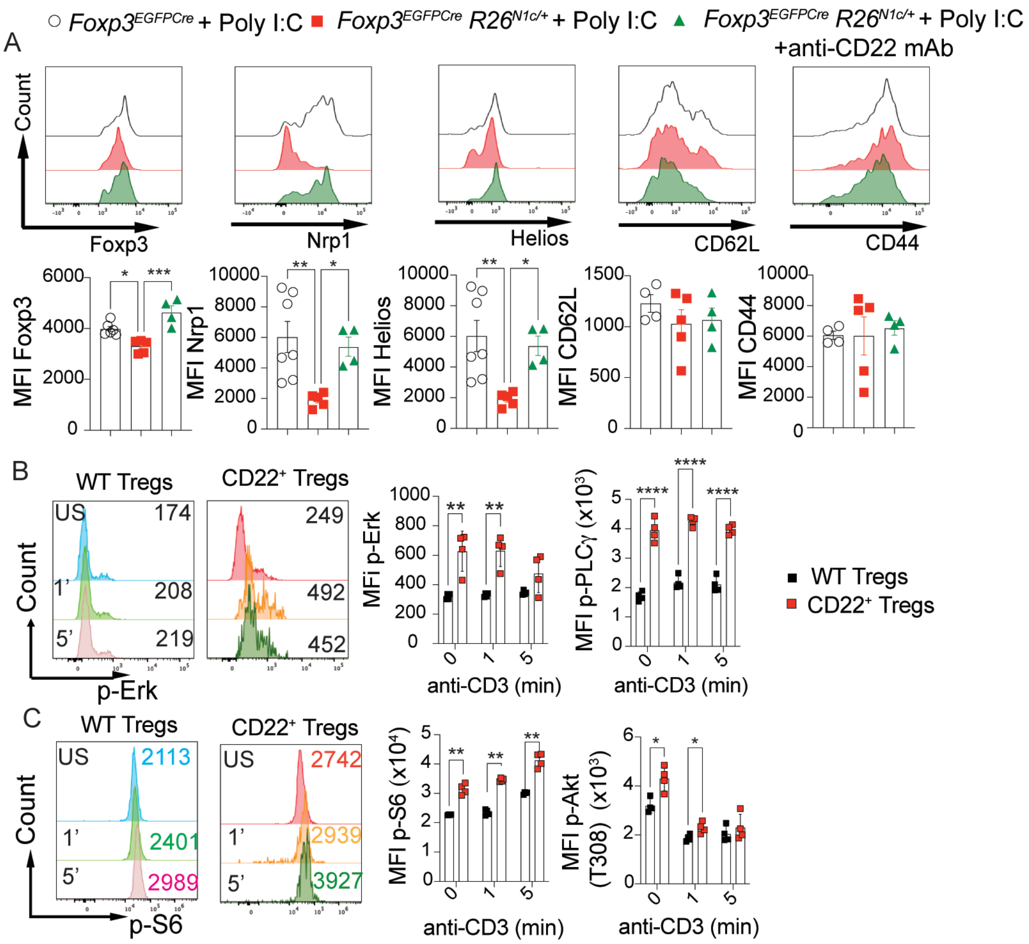

Figure 8: CD22 augments TCR signaling in Treg cells. A. Flow cytometric analysis and MFI of colonic Treg cell markers of Poly I: C-treated *Foxp3*$^{\text{EGFPCre}}$ and *Foxp3*$^{\text{EGFPCre}}$*R26*$^{\text{N1c/+}}$ mice co-treated with isotype control mAb or anti-CD22 mAb, as indicated. **B**. Flow cytometric analysis and MFI of p-Erk (**B**) and pPLC-γ expression induced by anti-CD3 mAb treatment of *Foxp3*$^{\text{EGFPCre}}$ and CD22^{+} *Foxp3*$^{\text{EGFPCre}}$*R26*$^{\text{N1c/+}}$Treg cells. **C**. Flow cytometric analysis and MFI of pS6 and p-T308-AKT expression induced by anti-CD3 mAb treatment of *Foxp3*$^{\text{EGFPCre}}$ and CD22^{+} *Foxp3*$^{\text{EGFPCre}}$*R26*$^{\text{N1c/+}}$Treg cells. Numbers in flow plots indicate percentages or MFI. Each symbol represents one mouse (A-C) Error bars indicate SEM. Statistical tests: One-way

ANOVA with Dunnett’s post hoc analysis (**A**), Two-way ANOVA with Sidak’s post hoc analysis (**B,C**)**;** *P<0.05, **P<0.01, ***P<0.001, ****P<0.0001.

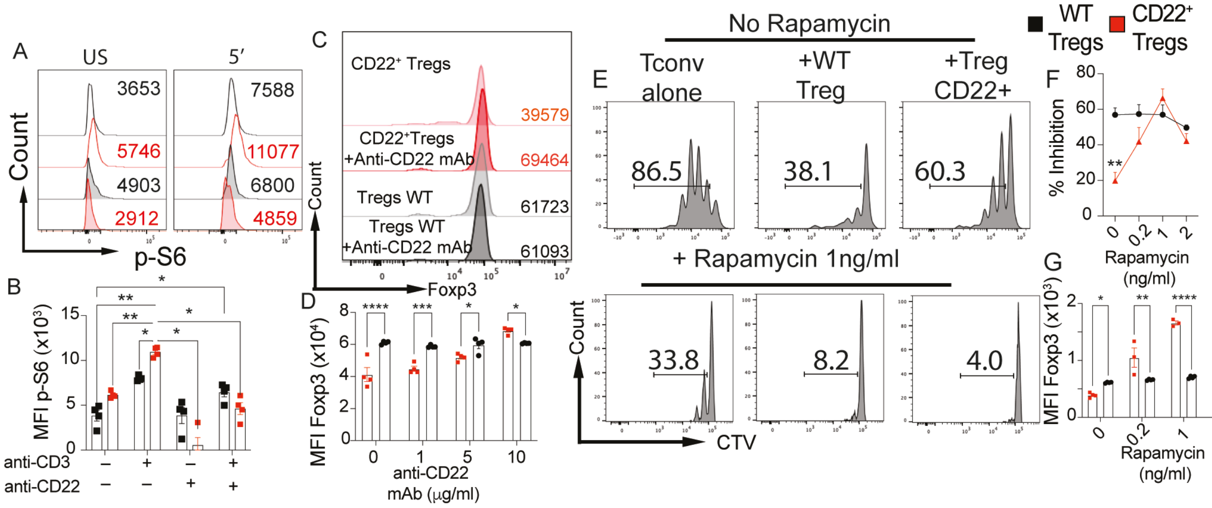

Figure 9: CD22 destabilizes Treg cells by an mTOR-dependent mechanism. A,B Flow cytometric analysis (A) and MFI (B) of pS6 expression induced by anti-CD3 mAb treatment of *Foxp3*$^{\text{EGFPCre}}$ and CD22^{+} *Foxp3*$^{\text{EGFPCre}}$*R26*$^{\text{N1c/+}}$Treg cells either treated or not with anti-CD22 mAb **C,D**. Foxp3 MFI in Treg from *In vitro* suppression of Tconv cell proliferation by *Foxp3*$^{\text{EGFPCre}}$ and CD22^{+} *Foxp3*$^{\text{EGFPCre}}$*R26*$^{\text{N1c/+}}$Treg cells in the presence of increasing concentrations of anti-CD22 mAb.. **E-F**. *In vitro* suppression of Tconv cell proliferation by *Foxp3*$^{\text{EGFPCre}}$ and CD22^{+} *Foxp3*$^{\text{EGFPCre}}$*R26*$^{\text{N1c/+}}$Treg cells in the presence of increasing concentrations of Rapamycin. **G**. Foxp3^{+} MFI in Treg cells from *In vitro* suppression of Tconv cell proliferation by *Foxp3*$^{\text{EGFPCre}}$ and CD22^{+} *Foxp3*$^{\text{EGFPCre}}$*R26*$^{\text{N1c/+}}$Treg cells in the presence of increasing concentrations of Rapamycin. Numbers in flow plots indicate percentages or MFI. Each symbol represents one mouse (A-G). Error bars indicate SEM. Statistical tests: Two-way ANOVA with Sidak's post hoc analysis (**B,D,F,G**); *P<0.05, **P<0.01, ***P<0.001, ****P<0.0001.

Supplementary Figure Legends

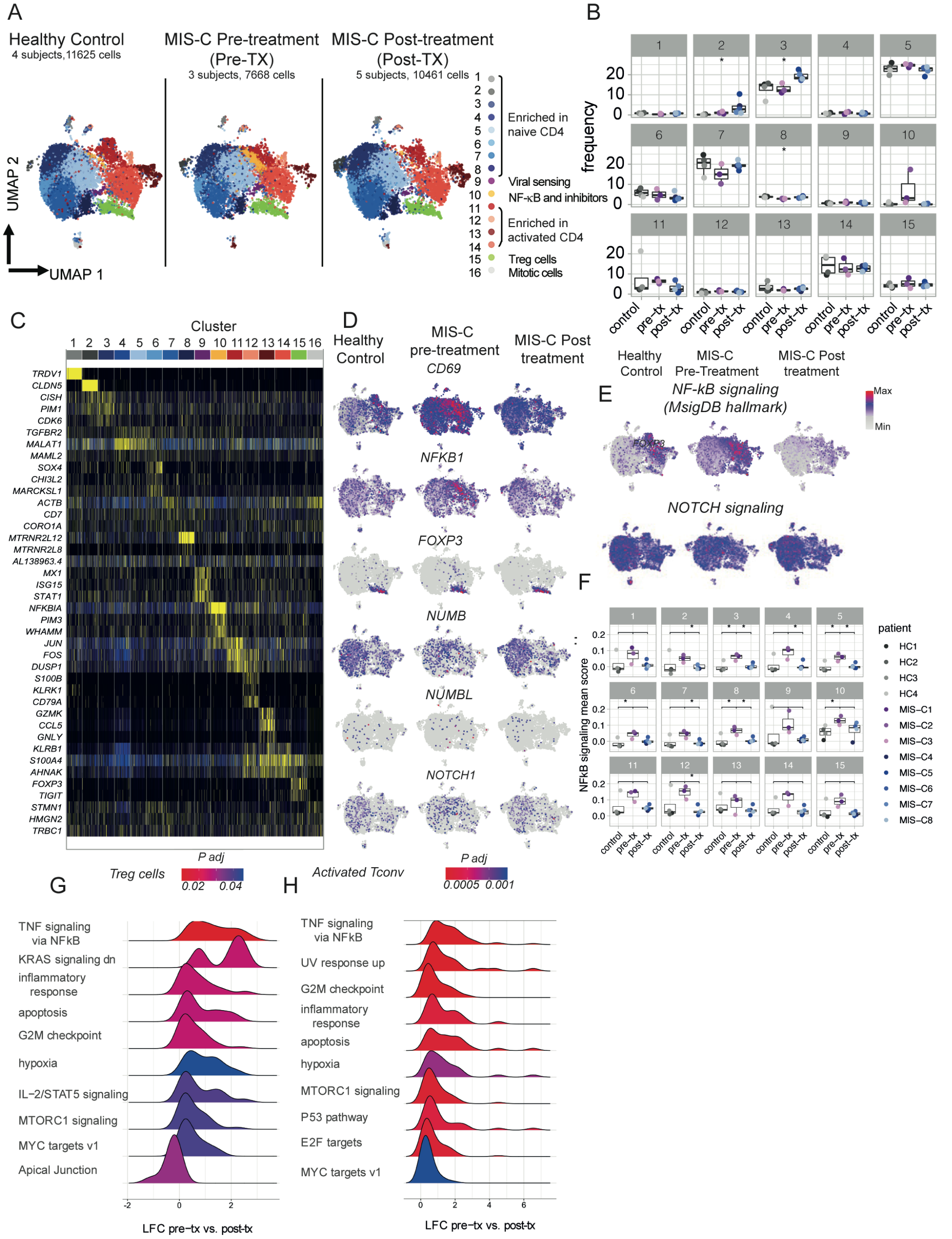

Fig. S1. Single-cell transcriptomic analyses of circulating CD4$^+$ T cells from control, pre- and post-treatment MIS-C subjects. A. Uniform manifold approximation and projection (UMAP) of normalized and harmonized dataset, split by disease group and color-coded by cluster. Clusters were delineated using Seurat. **B**. Frequencies (%) of each cluster among total CD4$^+$ T cells for each patient. **C**. Heatmap showing expression of the top genes in each cluster, as determined using Seurat. **D**. UMAP split by disease group and color-coded by expression of *CD69*, *NFKB1*, *FOXP3, NUMB, NUMBL and NOTCH1* at the single-cell level. **E.** UMAP split by disease group and color-coded by single-cell score for the TNFα signaling via NF-κB gene set (MSigDB Hallmark) and NOTCH signaling. **F**. TNFα signaling via NF-κB gene set mean score, averaged per cluster and patient. Multiple T-test comparisons significant at an FDR of 0.05 are indicated with a star. **G**, **H.** LFC distributions of genes belonging to each of the corresponding enriched hallmarks. Gene set enrichment analysis (GSEA) was run against the MSigDB hallmark database using ranked LFC derived from pseudobulk DEA of pre-treatment MIS-C versus control subjects in Tconv .

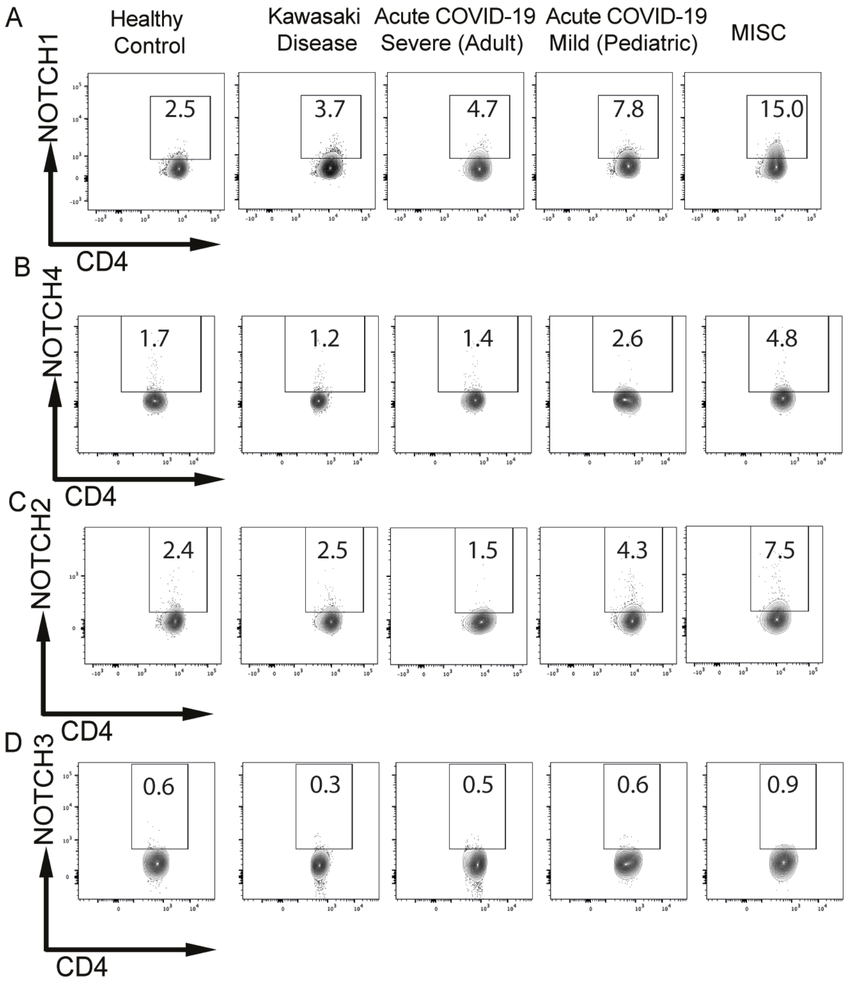

Figure S2: Flow cytometry analysis of Notches receptors expression on MISC Tconv: A-D. Flow cytometric analysis of Notch1 **(A)**, Notch4 **(B)**, Notch2 **(C)** and Notch3 **(D)** expression in CD4$^+$ Tconv cells of healthy control subjects, and patients with Kawasaki disease, adult subjects with severe COVID-19, pediatric subjects with mild or severe COVID-19 and MIS-C subjects.

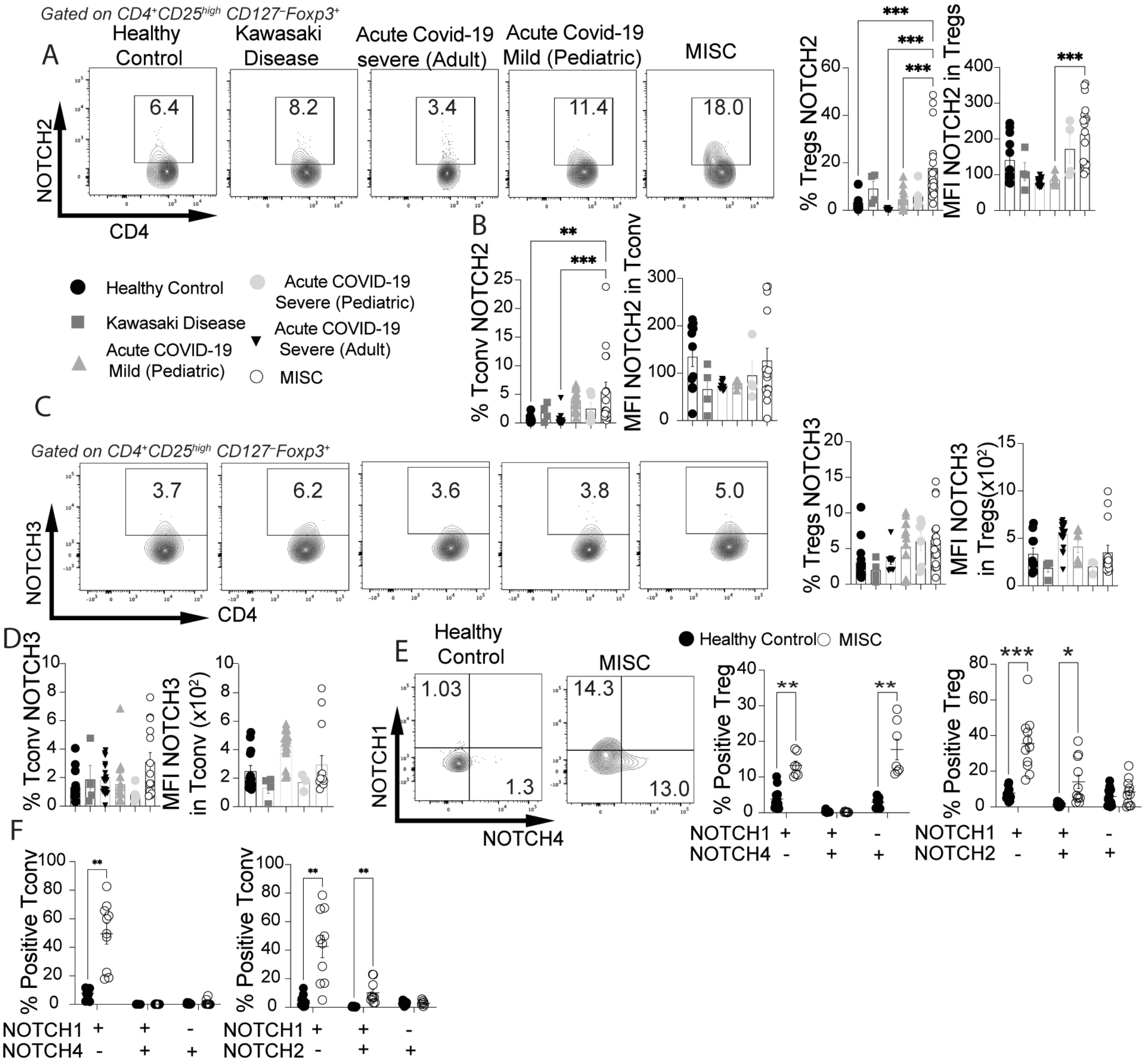

Fig. S3. **Notch receptor expression on circulating CD4⁺ Treg and Tconv cells in MIS-C**. **A to D.** Flow cytometric analysis, cell frequencies and mean fluorescence intensity (MFI) of Notch2 (**A,B**) and Notch3 expression (**C,D**) in CD4⁺ Treg and Tconv cells of healthy control subjects, and patients with Kawasaki disease, adult subjects with severe COVID-19, pediatric subjects with mild or severe COVID-19 and MIS-C subjects. **E-F.** Flow cytometric analysis, and cell frequencies of co-expression of Notch1 and Notch2 and Notch1 and Notch4 on circulating Treg cells (E) and Tconv (F) of MIS-C subjects**.**

Each symbol represents one subject. Numbers in flow plots indicate percentages. Error bars indicate SEM. Statistical tests: *P<0.05, **P<0.01, ***P<0.001, ****P<0.0001 by one-way ANOVA with Dunnett's post hoc analysis (**A to F**).

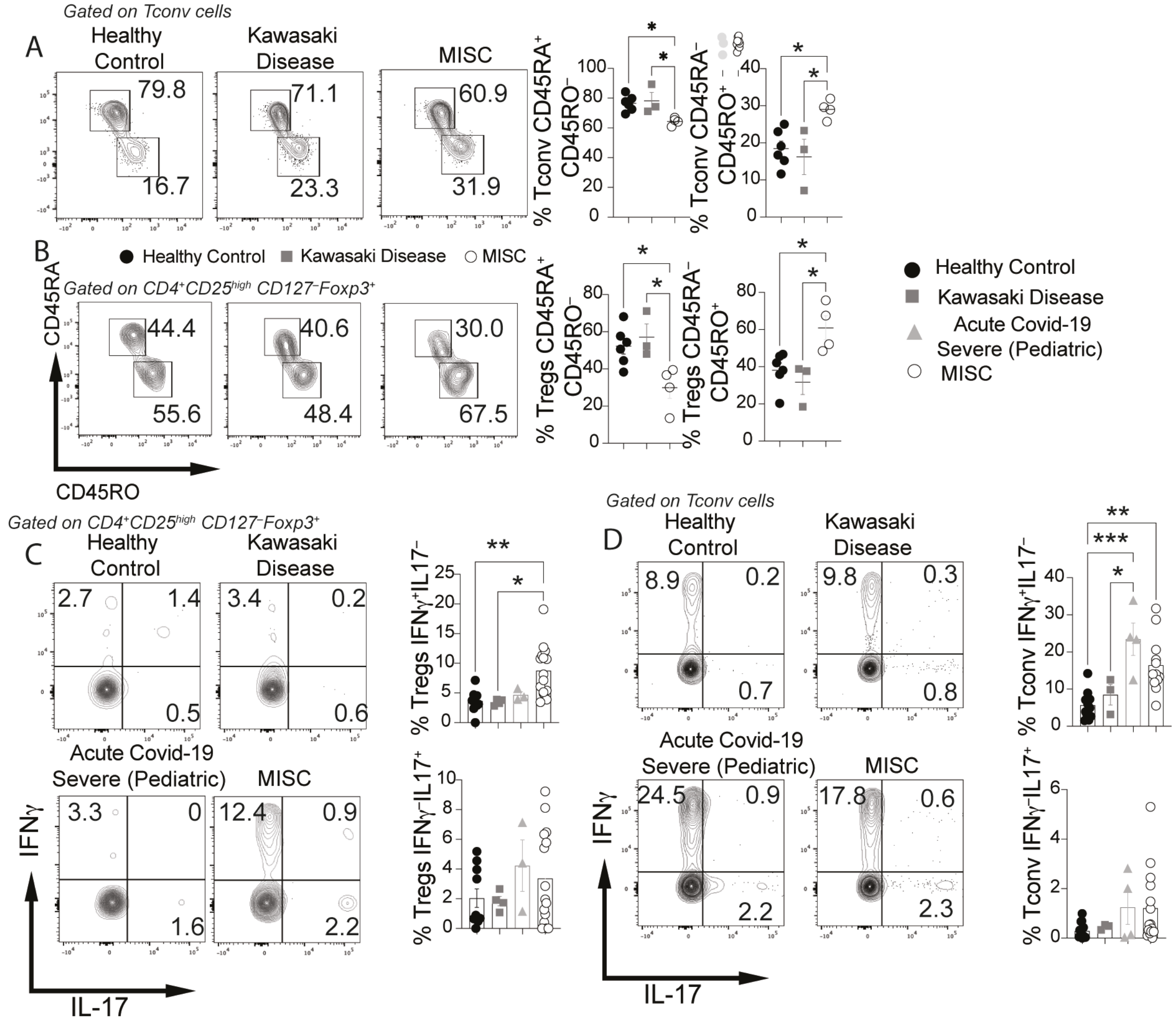

Fig. S4. **Characterization of circulating CD4$^+$ Treg and Tconv cells in MIS-C**. **A,B**. Flow cytometric analysis and cell frequencies of T cell activation state markers (CD45RA, CD45RO) on Tconv (**A**) and Treg (**B**) cells of the respective subject groups. **C and D.** Flow cytometric analysis and frequencies of IFNγ and IL-17-expressing Treg (**C**) and Tconv (**D**) cells of the respective subject groups. Each symbol represents one subject. Numbers in flow plots indicate percentages. Error bars indicate SEM. Statistical tests: *P<0.05, **P<0.01, ***P<0.001, ****P<0.0001 by one-way ANOVA with Dunnett's post hoc analysis (**A to D**).

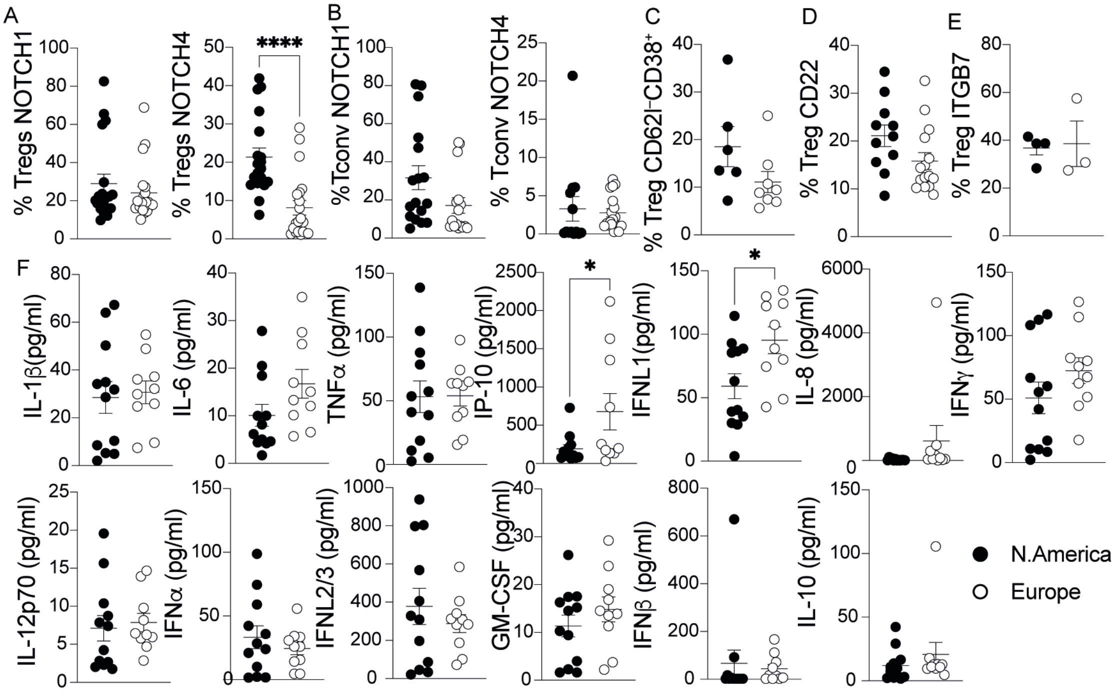

Figure S5: Comparison of MISC patients' characteristics based on the country of residency: **A**-**B**. Cell frequencies of Notch1 and Notch4 expression in CD4$^+$ Treg (**A**) and Tconv cells (**B**) of MISC from North America or Europe. **C,D,E**. Cell frequencies of mucosally imprinted (CD62l$^-$CD38$^+$) (**C**), CD22 (**D**) and ITGB7 (**E**) on Treg cells form the respective groups. **F**. serum concentrations of IL-1β, IL-6, TNF, IP-10, IFNL1, IL-8, IL12p70, IFNα, IFNλ2/3, IFNγ and IL-10, in the respective patient group subjects. Each symbol represents one subject. Error bars indicate SEM. Statistical tests: *$P<0.05$, ****$P<0.0001$ by student-t-test (**A and F**).

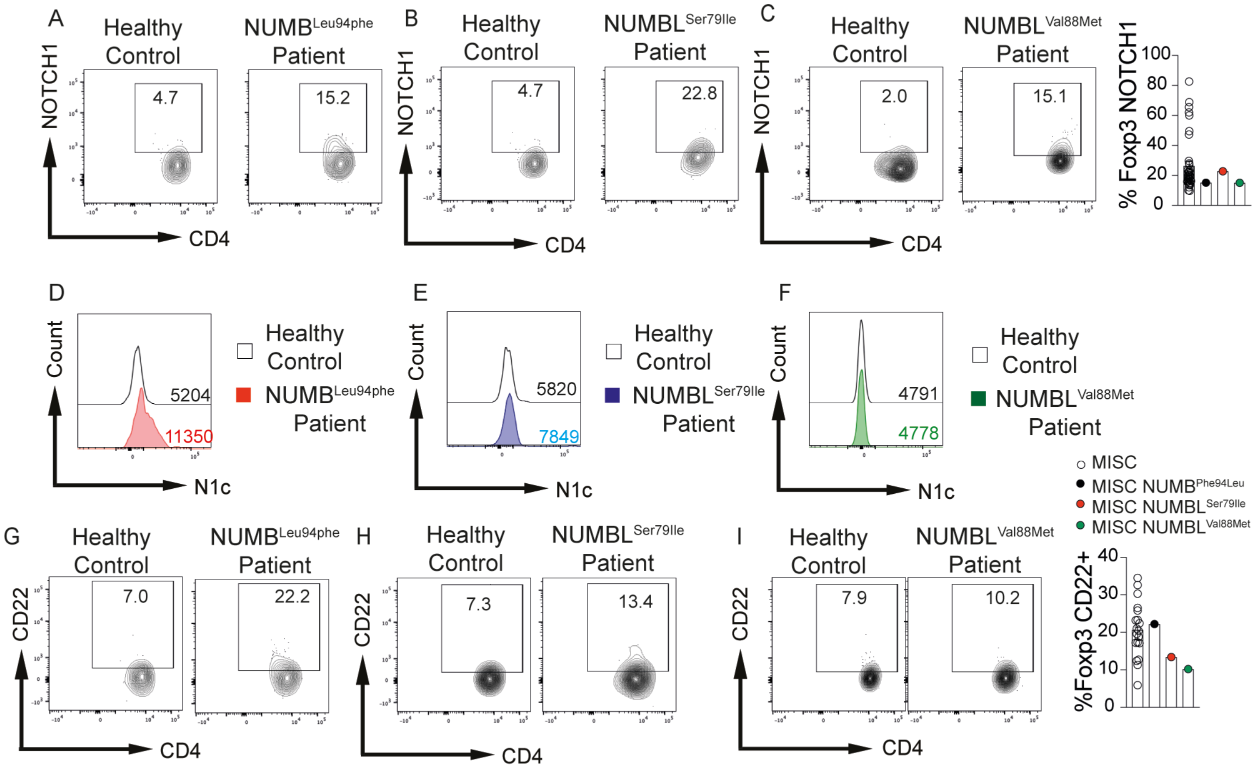

Fig. S6: Characterization of circulating CD4^{+} Treg in MIS-C with specific mutation in NUMB/NUMBL. A to I. Flow cytometric analysis and cell frequencies of Notch1 (**A to C**), N1c expression (**D to F**) and CD22 (**G to I**) in CD4^{+} Treg of healthy control subjects, and MIS-C patients with a specific mutation in NUMB^{leu94phe} (**A,D,G**), NUMBL^{Ser79Ile} (**B,E,H**) and NUMBL^{Val88Met} (**C, F, I**).

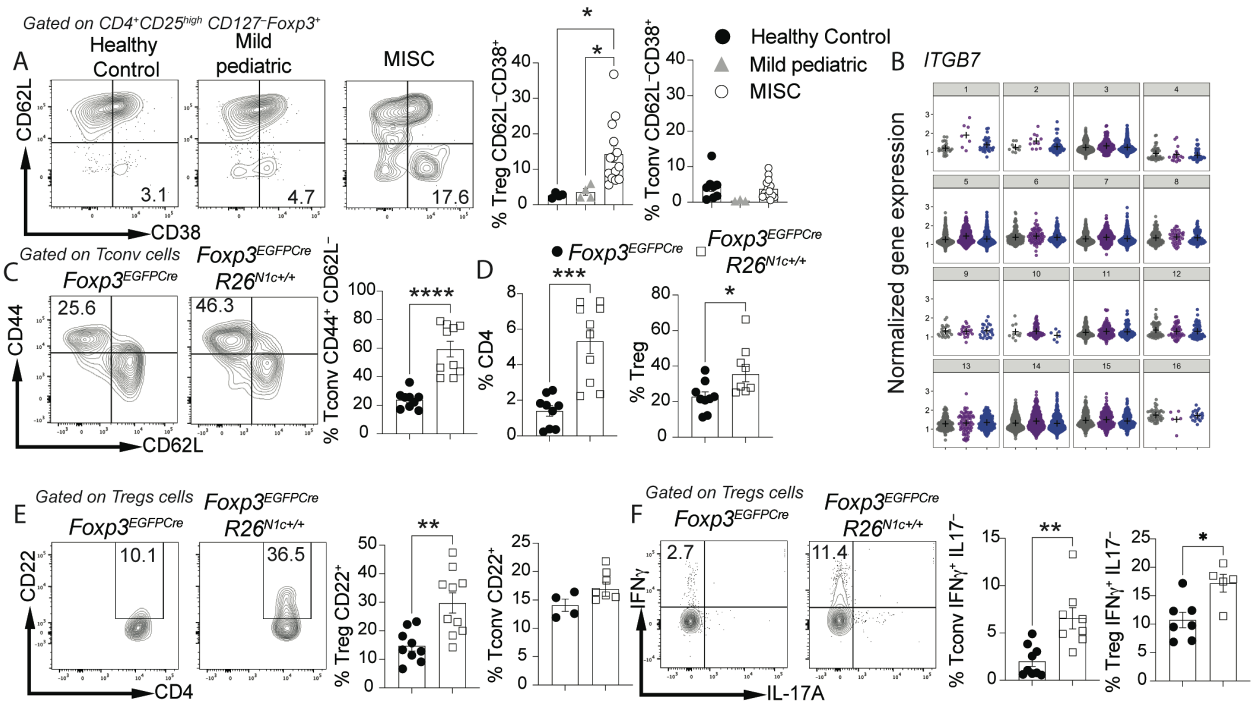

Fig. S7: Attributes of mucosal T cells in MIS-C and Poly I:C-treated *Foxp3*$^{\text{EGFPCre}}$*R26*$^{\text{N1c/+}}$ mice. **A**. Flow cytometric analysis and graphical representation of mucosal imprinted (CD62L^{-}CD38^{+}) Treg and Tconv cells in healthy control subjects, pediatric subjects with mild Covid-19 and MIS-C patients. **B**. Relative *ITGB7* gene expression in cell clusters of healthy control subjects (gray) and in MIS-C patients pre (purple) and post-treatment (blue) inferred from scRNA-seq analysis. **C and D**. Flow cytometric analysis and graphical representation of colonic T cell (CD3^{+}CD4^{+}), Treg (CD3^{+}CD4^{+}Foxp3^{+}) and activated Tconv (CD4^{+}CD44^{+}CD62L^{-}) cells of *Foxp3*$^{\text{EGFPCre}}$ and *Foxp3*$^{\text{EGFPCre}}$*R26*$^{\text{N1c/+}}$ mice subjected to Poly I:C treatment. **E**. Flow cytometric analysis and graphical representation of colonic CD22^{+} Treg and Tconv cells of *Foxp3*$^{\text{EGFPCre}}$ and *Foxp3*$^{\text{EGFPCre}}$*R26*$^{\text{N1c/+}}$ mice subjected to Poly I:C treatment. **F**. Flow cytometric analysis and graphical representation of IFNγ and IL-17 expressing Tconv and Treg cells of *Foxp3*$^{\text{EGFPCre}}$ and *Foxp3*$^{\text{EGFPCre}}$*R26*$^{\text{N1c/+}}$ mice subjected to Poly I:C treatment. Each symbol represents one human subject (**A**), one cell (**B**) or one mouse (**C to F**). Numbers in flow plots indicate percentages. Error bars indicate SEM. Statistical tests: One-way ANOVA with Dunnett's post hoc analysis (**A,C to F**) Two-way ANOVA with Sidak's post hoc analysis (**B**)**;**. *P<0.05, **P<0.01, ***P<0.001, ****P<0.0001.

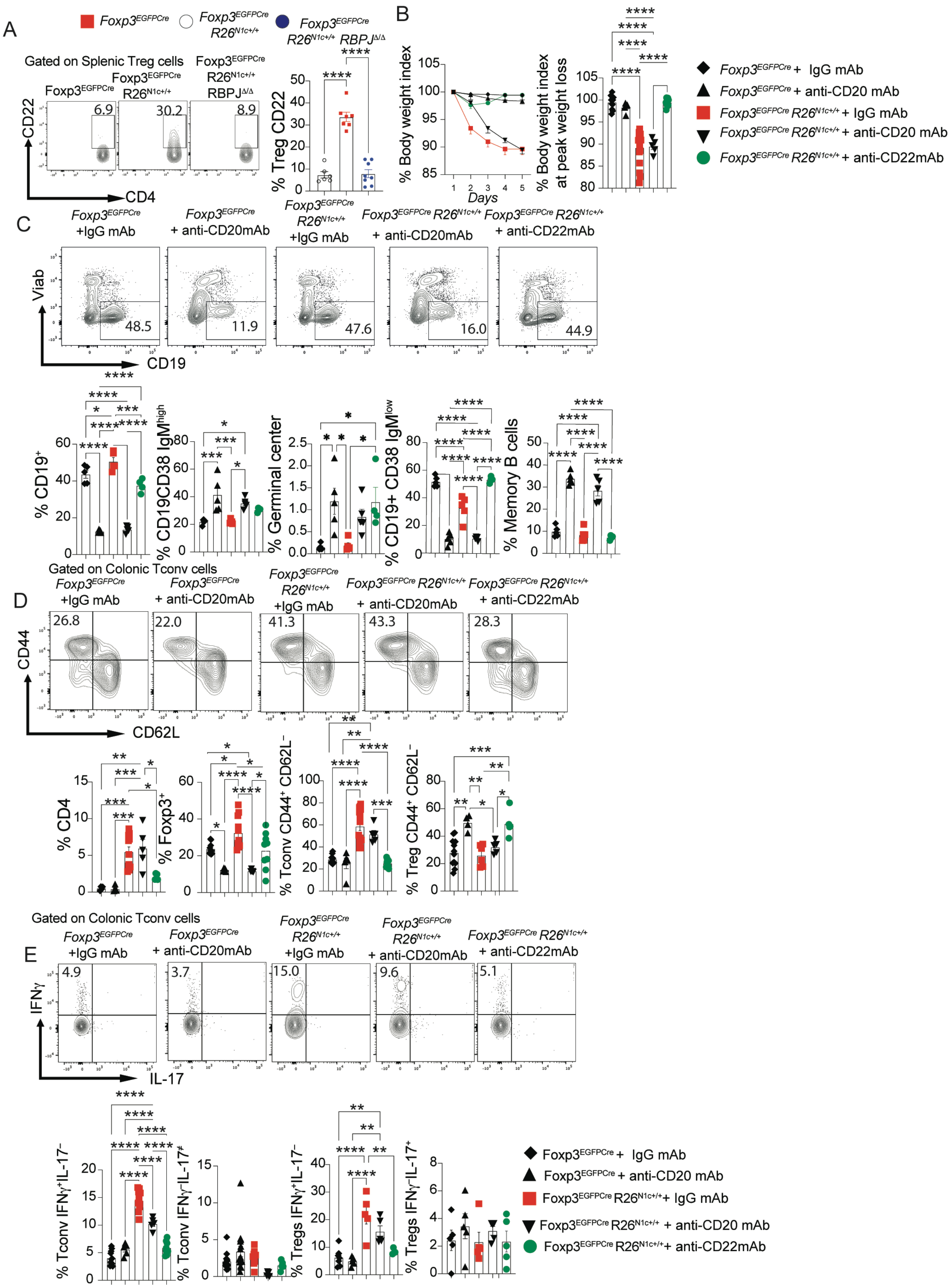
A
Foxp3EGFPCre
Foxp3EGFPCre R26N1c+/+
Foxp3EGFPCre R26N1c+/+ RBPJΔ/Δ
Gated on Splenic Treg cells
6.9
30.2
8.9
CD22
CD4
% Treg CD22
****
B
% Body weight index
Days
% Body weight index at peak weight loss
Foxp3EGFPCre + IgG mAb
Foxp3EGFPCre + anti-CD20 mAb
Foxp3EGFPCre R26N1c+/+ + IgG mAb
Foxp3EGFPCre R26N1c+/+ + anti-CD20 mAb
Foxp3EGFPCre R26N1c+/+ + anti-CD22mAb
C
Foxp3EGFPCre +IgG mAb
Foxp3EGFPCre + anti-CD20mAb
Foxp3EGFPCre R26N1c+/+ +IgG mAb
Foxp3EGFPCre R26N1c+/+ + anti-CD20mAb
Foxp3EGFPCre R26N1c+/+ + anti-CD22mAb
Viab
CD19
48.5
11.9
47.6
16.0
44.9
% CD19+
% CD19CD38 IgMhigh
% Germinal center
% CD19+ CD38 IgMlow
% Memory B cells
D
Gated on Colonic Tconv cells
CD44
CD62L
26.8
22.0
41.3
43.3
28.3
% CD4
% Foxp3+
% Tconv CD44+ CD62L−
% Treg CD44+ CD62L−
E
Gated on Colonic Tconv cells
IFNγ
IL-17
4.9
3.7
15.0
9.6
5.1
% Tconv IFNγ+IL-17−
% Tconv IFNγ−IL-17+
% Tregs IFNγ+IL-17−
% Tregs IFNγ−IL-17+
Foxp3EGFPCre + IgG mAb
Foxp3EGFPCre + anti-CD20 mAb
Foxp3EGFPCre R26N1c+/+ IgG mAb
Foxp3EGFPCre R26N1c+/+ + anti-CD20 mAb
Foxp3EGFPCre R26N1c+/+ anti-CD22mAb

Fig. S8. Anti-CD22 mAb therapy of Poly I:C-induced disease in *Foxp3*$^{\text{EGFPCre}}$*R26*$^{\text{N1c/+}}$ mice is B cell-independent. A. Flow cytometric analysis and frequencies of CD22 expression in Treg cells of *Foxp3*$^{\text{EGFPCre}}$, *Foxp3*$^{\text{EGFPCre}}$*Notch1c*$^{+/-}$ and *Foxp3*$^{\text{EGFPCre}}$*Notch1c*$^{+/-}$*RBPJ*$^{\Delta/\Delta}$ mice. **B.** Weight indices of Poly I:C treated *Foxp3*$^{\text{EGFPCre}}$ and *Foxp3*$^{\text{EGFPCre}}$*R26*$^{\text{N1c/+}}$ mice co-injected with anti-CD22 mAb or with an anti-CD20mAb. **C**. Flow cytometric analysis and graphical representation of different splenic B cell populations [CD19$^+$, CD19$^+$CD38$^+$IgM$^{\text{high}}$, germinal B cells (GL7$^+$), CD19$^+$CD38+IgM$^{\text{low}}$ and memory B cells (IgD$^-$CD27$^+$)] of *Foxp3*$^{\text{EGFPCre}}$ and *Foxp3*$^{\text{EGFPCre}}$*R26*$^{\text{N1c/+}}$ mice subjected to Poly I:C treatment. **D**. Flow cytometric analysis and graphical representation of colonic T cell (CD3$^+$CD4$^+$), Treg cells (CD3$^+$CD4$^+$Foxp3$^+$) and activated Tconv (CD4$^+$CD44$^+$CD62L$^-$) of Poly I:C treated *Foxp3*$^{\text{EGFPCre}}$ and *Foxp3*$^{\text{EGFPCre}}$*R26*$^{\text{N1c/+}}$ mice co-injected with anti-CD22 mAb or with an anti-CD20mAb. **E**. Flow cytometric analysis and graphical representation of IFNγ and IL-17 expressing colonic Tconv and Treg cells of Poly I:C treated *Foxp3*$^{\text{EGFPCre}}$ and *Foxp3*$^{\text{EGFPCre}}$*R26*$^{\text{N1c/+}}$ mice co-injected with anti-CD22 mAb or with an anti-CD20mAb. Numbers in flow plots indicate percentages. Error bars indicate SEM. Statistical tests: One-way ANOVA with Dunnett's post hoc analysis (**A, C to E**), Two-way ANOVA with Sidak's post hoc analysis (**B**); $^*P<0.05$, $^{**}P<0.01$, $^{***}P<0.001$, $^{****}P<0.0001$.

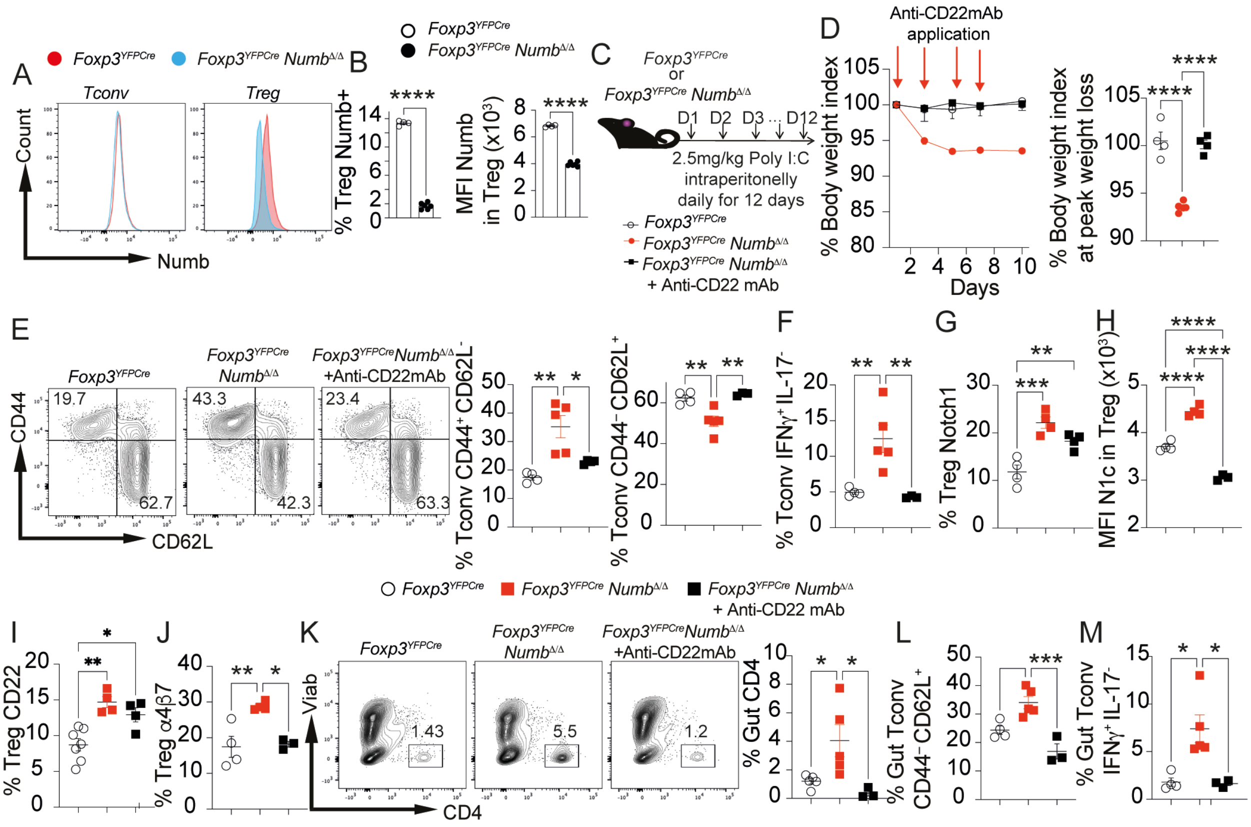

Fig. S9: Poly I:C-induced multiorgan inflammatory disease in *Foxp3*$^{\text{YFPCre}}$*NUMB*$^{\Delta/\Delta}$ mice. **A.** Flow cytometric analysis of Numb expression in Tconv and Treg cells from *Foxp3*$^{\text{YFPCre}}$ and *Foxp3*$^{\text{YFPCre}}$*Numb*$^{\Delta/\Delta}$ mice. **B.** Cell frequencies and MFI of Numb expression on Treg cells from the respective mice. **C**. Scheme of mouse Poly IC treatment. **D**. Body weight index change and peak weight loss of the *Foxp3*$^{\text{YFPCre}}$ and *Foxp3*$^{\text{YFPCre}}$*Numb*$^{\Delta/\Delta}$ mice treated with Poly IC alone or in combination with anti-CD22 mAb. **E and F**. Flow cytometric analysis and cell frequencies of CD44^{+}CD62L^{-} (**E**) and IFNγ^{+}IL-17^{-} Tconv cells (**F**). **G to J**. frequencies of Notch1^{+} (**G**), MFI of Notch1c^{+} (**H**), CD22 (**I**) and α4β7 (**J**) in Treg cells after Poly I:C treatment alone or in combination with anti-CD22 mAb. **K to M** Flow cytometric analysis and cell frequencies of Gut CD4 (**K**), of CD44^{+}CD62L^{-} (**L**) and IFNγ^{+}IL-17^{-} (**M**) gut Tconv cells. Numbers in flow plots indicate percentages. Error bars indicate SEM. Statistical tests: One-way ANOVA with Dunnett’s post hoc analysis (**B to H, J to M**); *P<0.05, **P<0.01, ***P<0.001, ****P<0.0001.

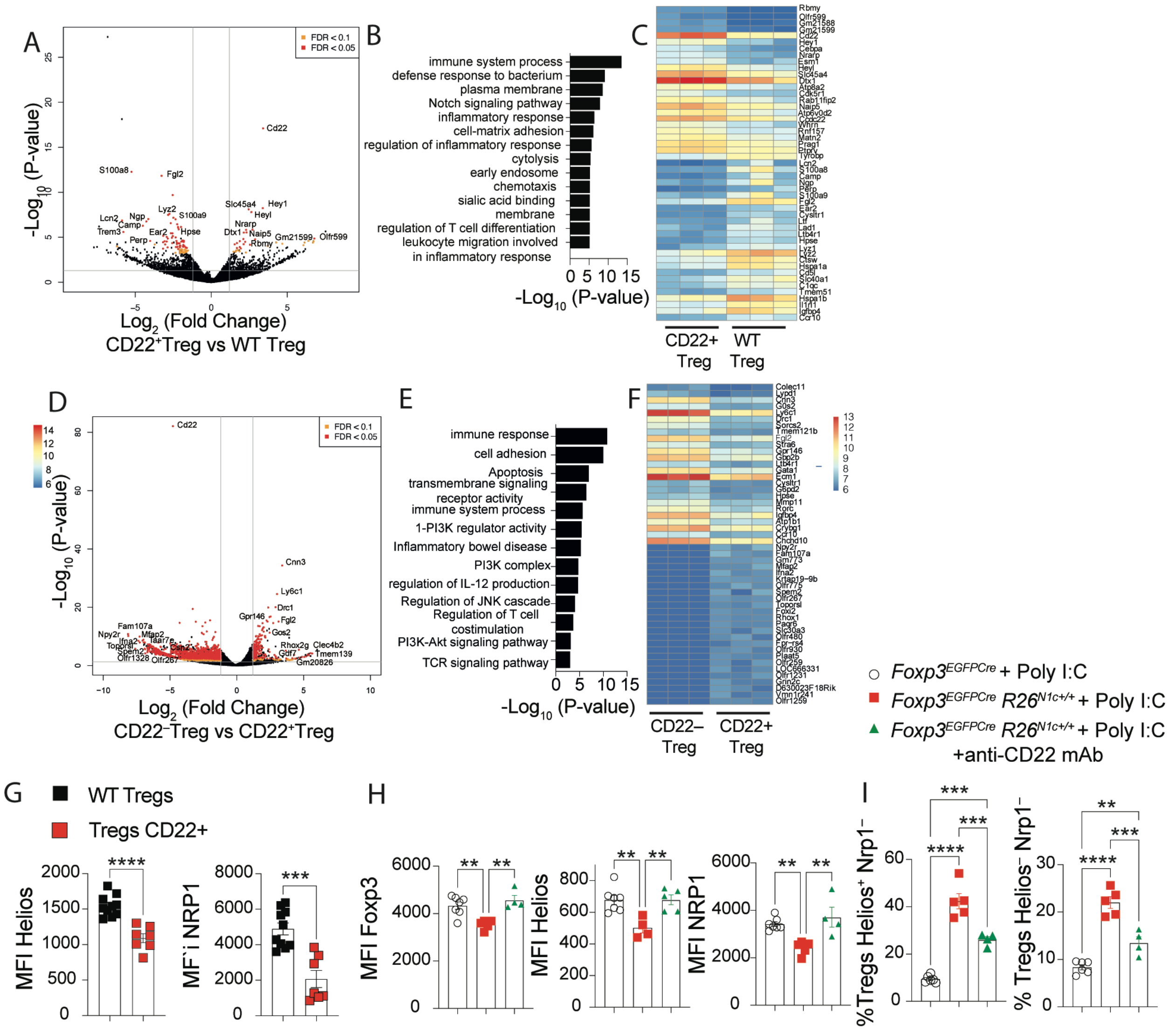

Fig. S10. Treg cell instability in Poly I:C-treated *Foxp3*$^{\text{EGFPCre}}$*R26*$^{\text{N1c/+}}$ mice. A to C, Volcano plot (A), pathway analysis (B) and heat map (C) of gene transcripts of WT or CD22+ Treg cells isolated at steady-state from *Foxp3*$^{\text{YFPCre}}$ and *Foxp3*$^{\text{EGFPCre}}$*R26*$^{\text{N1c/+}}$mice (n=3). **D to F**, Volcano plot (D), pathway analysis (E) and heat map (F) of gene transcripts of CD22^{-} or CD22^{+} Treg cells isolated at steady state from *Foxp3*$^{\text{EGFPCre}}$*R26*$^{\text{N1c/+}}$mice. **G,** MFI of splenic Treg cell markers of WT or CD22^{+} Treg cells isolated at steady state from *Foxp3*$^{\text{YFPCre}}$ and *Foxp3*$^{\text{EGFPCre}}$*R26*$^{\text{N1c/+}}$mice. **H,** Flow cytometric analysis and MFI of splenic Treg cell markers of Poly I:C-treated *Foxp3*$^{\text{EGFPCre}}$ and *Foxp3*$^{\text{EGFPCre}}$*R26*$^{\text{N1c/+}}$ mice co-treated with isotype control mAb or anti-CD22 mAb, as indicated. **I**, Cell frequencies of Helios and NRP1 expression on splenic Treg cells in the groups shown in (H). Each symbol represents one mouse. Error bars indicate SEM. Statistical tests: Student-t-test (G), One-way ANOVA with Dunnett's post hoc analysis (H,**I**);**;** **P<0.01, ***P<0.001, ****P<0.0001.

Table S1: Clinical characteristics of patient and control subjects.

	MIS-C **N=45**	**Pedi COVID-19** **N=50**	**KD** **N=5**	**Pedi Controls** **N=18**
Patient Demographics				
Age-yrs (median, IQR)	8.0, 5.0-12.4	13.0, 3.0-16.0	7.0, 1.5-10.5	3.5, 1.0-5.8
Sex (#, % female)	30, 68%	24, 48%	2, 40%	6, 33%
Race & Ethnicity (#, %)				
White, non-Hispanic	25, 56%	43, 86%	3, 60%	15, 83%
Black, non-Hispanic	4, 9%	0, 0%	0, 0%	0, 0%
Hispanic	9, 20%	4, 8%	1, 20%	2, 11%
Asian	0, 0%	0, 0%	1, 20%	1, 6%
Other	2, 4%	1, 2%	0, 0%	0, 0%
Unknown	5, 11%	2, 4%	0, 0%	0, 0%
Pre-existing Conditions (#, %)	15, 33%	7, 14%	2, 40%	0, 0%
BMI kg/m^2 (median, IQR)	19.3, 16.1-25.6	18.6, 16.9-23.8	17.0, 14.6-20.5	-
Case Definitions/Criteria (#, %)				
WHO MIS-C	42, 93%	-	-	-
CDC MIS-C	45, 100%	-	-	-
Complete KD Criteria	6, 13%	-	3, 60%	-
Incomplete KD Criteria	6, 13%	-	2, 40%	-
Clinical Features (#, %)				
Fever	45, 100%	36, 72%	5, 100%	-
Rash	22, 49%	1, 2%	5, 100%	-

Conjunctivitis	26, 58%	1, 2%	5, 100%	-
Mucositis	8, 18%	1, 2%	3, 60%	-
Extremity Changes	12, 27%	1, 2%	4, 80%	-
Lymphadenopathy	11, 24%	0, 0%	2, 40%	-
Shock	14, 31%	0, 0%	0, 0%	-
GI Symptoms	43, 96%	10, 20%	2, 40%	-
Abdominal Pain	28, 62%	4, 8%	1, 20%	-
Vomiting	30, 67%	5, 10%	2, 40%	-
Diarrhea	24, 53%	3, 6%	0, 0%	-
Respiratory Symptoms	18, 40%	27, 54%	0, 0%	-
Cough	4, 9%	19, 38%	0, 0%	-
Dyspnea	3, 7%	4, 8%	0, 0%	-
Hypoxia	9,20%	7, 14%	0, 0%	-
Infiltrate on Chest Imaging	5,11%	9, 18%	0, 0%	-
Neurologic Symptoms	6,13%	6, 12%	0, 0%	-
Headache	3,67%	3, 6%	0, 0%	-
Anosmia/Dysgeusia	0, 0%	2, 4%	0, 0%	-
Altered Mental Status	1, 2%	0, 0%	0, 0%	-
CN Palsy	0, 0%	0, 0%	0, 0%	-
Meningismus	1, 2%	0, 0%	0, 0%	-
Seizure	0, 0%	1, 2%	0, 0%	-
SARS-CoV-2 Testing (#, %)[*]				
PCR positive	16, 36%	50, 100%	0, 0%	-
Seropositive	41, 91%	6, 12%	0, 0%	-

Laboratory Features (median, IQR)				
Lowest ALC $x10^3$/mL	0.91, 0.53-1.35	1.8, 1.22-3.35	0.87, 0.65-2.57	-
Lowest Hgb g/dL	10.0, 9.2-10.7	12.6, 10.9-13.8	11.0, 8.2-12.1	-
Lowest Plt $x10^3$/mL	192, 126-236	269, 207-353	340, 156-414	-
Highest CRP mg/dL	16.0, 7.8-24.0	0.3, 0.1-6.3	5.8, 4.1-21.3	-
Highest Ferritin ng/mL	502, 305-1134	143, 70-326	175, 134-779	-
Highest D-dimer mcg/mL	3.1, 1.5-6.2	0.8, 0.5-1.4	1.7, 1.2-3.9	-
Highest ALT U/L	40, 22-79	31, 17-48	50, 41-133	-
Highest Cr mg/dL	0.47, 0.39-0.61	0.54, 0.26-0.68	0.34, 0.27-0.60	-
Highest BNP pg/mL	1118, 185-2150	34, 13-130	35, 13-422	-
Highest Troponin ng/mL	0.02, 0.01-0.11	0.01, 0.01-0.02	0.01, 0.01-0.01	-
Cardiovascular Features (#, %)▲				
EF <55%	16, 36%	-	0, 0%	-
Coronary Artery Dilation	3, 7%	-	0, 0%	-
Coronary Artery Aneurysm	3, 7%	-	2, 40%	-
Clinical Interventions (#, %)				
ICU Admission	14, 31%	2, 4%	0, 0%	-
Vasopressors	9, 20%	0, 0%	0, 0%	-
Supplemental O2	8, 18%	8, 16%	0, 0%	-
CPAP	0, 0%	3, 6%	0, 0%	-
BiPAP	5, 11%	1, 2%	0, 0%	-
Mechanical Ventilation	1, 2%	0, 0%	0, 0%	-

Immunomodulatory Treatments (#, %)▼				
Any Immunomodulatory Treatment	41, 91%	3, 6%	4, 80%	-
IVIG	37, 82%	1, 2%	4, 80%	-
Glucocorticoids	31, 69%	2, 4%	2, 40%	-
Anakinra	5, 11%	0, 0%	1, 20%	-
Other	3, 7%	0, 0%	0, 0%	-

MIS-C, multisystem inflammatory syndrome in children; pedi, pediatric; COVID-19, coronavirus disease 2019; KD, Kawasaki disease; yrs, years; WHO, World Health Organization; CDC, Centers for Disease Control and Prevention; GI, gastrointestinal; CN, cranial nerve; PCR, polymerase chain reaction; ALC, absolute lymphocyte count; Hgb, hemoglobin; Plt, platelet count; CRP, C-reactive protein; ALT, alanine aminotransferase; Cr, creatinine; BNP, B-type natriuretic peptide; EF, ejection fraction; ICU, intensive care unit; O2, oxygen; CPAP, continuous positive airway pressure; bilevel positive airway pressure; IVIG, intravenous immunoglobulin

*42/45 MIS-C patients were PCR tested for SARS-CoV-2. 44/45 MIS-C patients underwent serologic testing for SARS-CoV-2. All children with acute COVID-19 had PCR testing and 8 had serologic testing. All KD patients had PCR and serologic testing.

▲All children with MIS-C and KD had an echocardiogram preformed.

▼Immunomodulatory treatment before biosample collection. Pre-treatment samples were obtained from 5/33 MIS-C and 1/5 KD patients.

Table S2: Antibodies used for flow cytometry

Mouse antibodies			
Markers	company	catalogue	Clone
Foxp3	Thermofisher	48-5773-82	FJK-16S
IFNγ	Biolegend	505825	XMG1.2
Helios	Thermofisher	47-9883-42	22F6
CD4	Biolegend	100451	GK1.5
CD3	Biolegend	100203	17A2
IL-17	Biolegend	506922	TC11-18H10.1
CD45	Biolegend	103140	30-F11
Notch4	Biolegend	128407	HMN4-14
CD279	Thermofisher	12-9985-82	J43
CD44	Biolegend	103032	IM7
CD62L	Biolegend	104412	MEL-14
N1c	Biolegend	629106	mN1A
α4β7	Biolegend	120606	DATK32
p-Erk	Biolegend	369506	6B8B69
p-PLCγ	Biolegend	612404	A17025A
pS6	CST	5316	D57.2.2E
p-Akt^{s473}	BD	560378	M89-61
p-Akt^{T308}	BD	558375	J1-223.371
CD22	Biolegend	126112	OX-97
Human antibodies			
CD3	Biolegend	300318	HIT3a,

CD4	Biolegend	300530	RPA-T4
Foxp3	Thermofisher	48-4776-42,56-4716-41	PCH-101
Notch1	BD Pharmingen	566023	HMN1-519
Notch2	BD Pharmingen	742291	HMN2-25
Notch3	BD Pharmingen	744828	HMN3-21
Notch4	BD Pharmingen	563269	HMN4-2
CD25	Thermofisher	12-0259-42	BC96
CD127	Biolegend	351320	A019D5
IFNγ	BD Biosciences	560741	4S.B3
ITGB7	BD	551082	FIB504
CCR7	Biolegend	353208	G043H7
CD38	Biolegend	397114	S17015A
CD22	Biolegend	302516	HIB22
CD45RA	Biolegend	304134	HI100
CD45RO	Biolegend	304236	UCHL1
IL17	Biolegend	512315	BL168
CD62L	Biolegend	304810	DREG-56
Purified anti-CD22	Biolegend	302502	HIB22

Overcoming COVID-19 Investigators

(Listed in PubMed, and ordered by U.S. State)

The following study group members were all closely involved with the design, implementation, and oversight of the Overcoming COVID-19 study.

Alabama: Children's of Alabama, Birmingham. Michele Kong, MD.

Arizona: University of Arizona, Tucson. Mary Glas Gaspers, MD; Katri V. Typpo, MD.

Arkansas: Arkansas Children's Hospital, Little Rock. Ronald C. Sanders Jr., MD, MS; Katherine Irby, MD.

California: Children's Hospital of Orange County, Orange County. Adam J. Schwarz, MD.

California: Miller Children's & Women's Hospital Long Beach, Long Beach. Christopher J. Babbitt, MD.

California: UCSF Benioff Children's Hospital Oakland, Oakland. Natalie Z. Cvijanovich, MD.

California: UCSF Benioff Children's Hospital, San Francisco. Matt S. Zinter, MD

Colorado: Children's Hospital Colorado, Aurora. Aline B. Maddux, MD, MSCS; Peter M. Mourani, MD.

Connecticut: Connecticut Children's, Hartford. Christopher L. Carroll, MD, MS.

Connecticut: Yale New-Haven Children's Hospital, New Haven. John S. Giuliano, Jr., MD.

Florida: Holtz Children's Hospital, Miami. Gwenn E. McLaughlin, MD, MSPH.

Georgia: Children's Healthcare of Atlanta at Egleston, Atlanta. Keiko M. Tarquinio, MD.

Illinois: Ann & Robert H. Lurie Children's Hospital of Chicago, Chicago. Kelly N. Michelson, MD, MPH; Bria M. Coates, MD.

Indiana: Riley Hospital for Children, Indianapolis. Courtney M. Rowan, MD, MS.

Iowa: University of Iowa Stead Family Children’s Hospital, Iowa City. Kari Wellnitz, MD; Guru Bhoojhawon MBBS, MD.

Kentucky: University of Louisville and Norton Children’s Hospital, Louisville, Janice E. Sullivan, MD; Vicki L.Montgomery, MD; Kevin M. Havlin, MD.

Louisiana: Children's Hospital of New Orleans, New Orleans. Tamara T. Bradford, MD.

Maryland: Johns Hopkins Children’s Hospital, Baltimore. Becky J. Riggs,MD; Melania M. Bembea, MD, MPH, PhD.

Maryland: University of Maryland Children’s Hospital, Baltimore. Ana Lia Graciano, MD.

Maryland: Sinai Hospital of Baltimore, Baltimore. Susan V. Lipton, MD, MPH.

Massachusetts: Baystate Children’s Hospital, Springfield. Kimberly L. Marohn, MD.

Massachusetts: Boston Children’s Hospital, Boston. Adrienne G. Randolph, MD; Margaret M. Newhams, MPH; Sabrina R. Chen; Cameron C. Young; Suden Kucukak, MD; Katherine Kester; Jane W. Newburger, MD, MPH; Kevin G. Friedman, MD; Mary Beth F. Son, MD; Janet Chou, MD.

Massachusetts: Mass General Hospital for Children, Boston. Ryan W. Carroll, MD, MPH; Phoebe H. Yager, MD; Neil D. Fernandes, MBBS.

Michigan: Children’s Hospital of Michigan, Detroit. Sabrina M. Heidemann, MD.

Michigan: University of Michigan CS Mott Children’s Hospital, Ann Arbor. Heidi R. Flori, MD, FAAP.

Minnesota: University of Minnesota Masonic Children’s Hospital, Minneapolis, Janet R. Hume, MD, PhD.

Minnesota: Mayo Clinic, Rochester. Emily R. Levy, MD.

Mississippi: Children’s Hospital of Mississippi, Jackson. Charlotte V. Hobbs, MD.

Missouri: Children’s Mercy Hospital, Kansas City. Jennifer E. Schuster, MD.

Missouri: Washington University in St. Louis. Philip C. Spinella MD.

Nebraska: Children’s Hospital & Medical Center, Omaha. Melissa L. Cullimore, MD, PhD; Russell J. McCulloh, MD.

New Jersey: Hackensack University Medical Center, Hackensack. Katharine N. Clouser, MD.

New Jersey: Newark Beth Israel Medical Center, Newark. Rowan F. Walsh, MD

New Jersey: Bristol-Myers Squibb Children's Hospital, New Brunswick. Lawrence C. Kleinman, MD, MPH,

FAAP; Simon Li, MD, MPH; Steven M. Horwitz, MD.

New Jersey: St. Barnabas Medical Center, Livingston. Shira J. Gertz, MD.

New York: Golisano Children’s Hospital, Rochester. Kate G. Ackerman, MD; Jill M. Cholette, MD.

New York: Kings County Hospital, Brooklyn. Michael A. Keenaghan, MD.

New York: Maria Fareri Children's Hospital, Valhalla. Aalok R. Singh, MD.

New York: The Mount Sinai Hospital, New York City. Sheemon P. Zackai, MD; Jennifer K. Gillen, MD.

New York: Hassenfeld Children’s Hospital at NYU Langone, New York. Adam J. Ratner, MD, MPH; Heda

Dapul, MD; Vijaya L. Soma, MD.

New York: Stony Brook University Hospital, Stony Brook. Ilana Harwayne-Gidansky, MD; Saul R. Hymes, MD.

New York: SUNY Downstate Medical Center University Hospital, Brooklyn. Sule Doymaz, MD.

North Carolina: University of North Carolina at Chapel Hill, Chapel Hill. Stephanie P. Schwartz, MD; Tracie C.

Walker, MD.

Ohio: University Hospitals Rainbow Babies and Children's Hospital, Cleveland. Steven L. Shein, MD; Amanda

N. Lansell, MD.

Ohio: Nationwide Children's Hospital, Columbus. Mark W. Hall MD, FCCM.

Ohio: Cincinnati Children's Hospital, Cincinnati. Mary A. Staat, MD, MPH.

Pennsylvania: Children's Hospital of Philadelphia, Philadelphia. Julie C. Fitzgerald, MD, PhD, MSCE; Jenny L.

Bush RN, BSN; Ryan H. Burnett, BS.

Pennsylvania: Penn State Children's Hospital, Hershey. Neal J. Thomas, MD, MSc.

Pennsylvania: St. Christopher's Hospital for Children, Philadelphia. Monica L. Koncicki, MD.

Pennsylvania: UPMC Children's Hospital of Pittsburgh. Ericka L. Fink, MD, MS; Joseph A. Carcillo, MD.

South Carolina: MUSC Children's Health, Charleston. Elizabeth H. Mack, MD, MS.; Laura Smallcomb, MD.

Tennessee: Monroe Carell Jr. Children's Hospital at Vanderbilt, Nashville. Natasha B. Halasa, MD, MPH.

Tennessee: Le Bonheur Children's Hospital, Memphis. Dai Kimura, MD.

Texas: Texas Children's Hospital, Houston. Laura L. Loftis, MD.

Texas: University of Texas Health Science Center, Houston. Alvaro Coronado Munoz, MD.

Texas: University of Texas Southwestern, Children's Medical Center Dallas, Dallas. Mia Maamari, MD; Cindy Bowens, MD, MSCS.

Utah: Primary Children's Hospital, Salt Lake City. Hillary Crandall, MD, PhD.

Washington: Seattle Children's Hospital, Seattle. Lincoln S. Smith, MD; John K. McGuire, MD.

CDC COVID-19 Response Team on Overcoming COVID-19: Manish M. Patel, MD, MPH; Leora R. Feldstein, PhD, MSc; Mark W. Tenforde, MD PhD; Ashley M. Jackson MPH; Nancy Murray MSc; Charles E. Rose, PhD.